Materials Science & Engineering C 118 (2021) 111433

Contents lists available at ScienceDirect

Materials Science & Engineering C

journal homepage: www.elsevier.com/locate/msec

3D printing of silk microparticle reinforced polycaprolactone scaffolds for tissue engineering applications

Cian Vyas[a,*,1], Jun Zhang[b,1], Øystein Øvrebø[c], Boyang Huang[a], Iwan Roberts[d], Mohan Setty[b], Benjamin Allardyce[b], Håvard Haugen[e], Rangam Rajkhowa[b], Paulo Bartolo[a,*]

[a] Department of Mechanical, Aerospace, and Civil Engineering, University of Manchester, UK
[b] Institute for Frontier Materials, Deakin University, Australia
[c] Department of Materials, Imperial College London, UK
[d] Department of Clinical Neurosciences, University of Cambridge, UK
[e] Institute of Clinical Dentistry, University of Oslo, Norway

ARTICLE INFO

Keywords:
3D printing
Silk microparticles
Tissue engineering
Scaffolds

ABSTRACT

Polycaprolactone (PCL) scaffolds have been widely investigated for tissue engineering applications, however, they exhibit poor cell adhesion and mechanical properties. Subsequently, PCL composites have been produced to improve the material properties. This study utilises a natural material, *Bombyx mori* silk microparticles (SMP) prepared by milling silk fibre, to produce a composite to enhance the scaffolds properties. Silk is biocompatible and biodegradable with excellent mechanical properties. However, there are no studies using SMPs as a reinforcing agent in a 3D printed thermoplastic polymer scaffold. PCL/SMP (10, 20, 30 wt%) composites were prepared by melt blending. Rheological analysis showed that SMP loading increased the shear thinning and storage modulus of the material. Scaffolds were fabricated using a screw-assisted extrusion-based additive manufacturing system. Scanning electron microscopy and X-ray microtomography was used to determine scaffold morphology. The scaffolds had high interconnectivity with regular printed fibres and pore morphologies within the designed parameters. Compressive mechanical testing showed that the addition of SMP significantly improved the compressive Young's modulus of the scaffolds. The scaffolds were more hydrophobic with the inclusion of SMP which was linked to a decrease in total protein adsorption. Cell behaviour was assessed using human adipose derived mesenchymal stem cells. A cytotoxic effect was observed at higher particle loading (30 wt%) after 7 days of culture. By day 21, 10 wt% loading showed significantly higher cell metabolic activity and proliferation, high cell viability, and cell migration throughout the scaffold. Calcium mineral deposition was observed on the scaffolds during cell culture. Large calcium mineral deposits were observed at 30 wt% and smaller calcium deposits were observed at 10 wt%. This study demonstrates that SMPs incorporated into a PCL scaffold provided effective mechanical reinforcement, improved the rate of degradation, and increased cell proliferation, demonstrating potential suitability for bone tissue engineering applications.

1. Introduction

3D printing technologies are enabling the development of complex multi-material structures for tissue engineering applications that are beginning to more accurately reflect the multifaceted biophysical environment within tissues [1,2]. The advancement of 3D printing or bioprinting is facilitating advancements in a range of tissue engineering applications such as bone, cartilage, cardiac, skin, vasculature, and the development of biomimetic disease models [3–8]. However, a key priority is the development of advanced biomaterials that are compatible with bioprinting technologies but also provide superior physical and biological properties. This is of utmost necessity in bone tissue engineering applications, which has a demanding set of requirements due to the complexity and remarkable properties exhibited by the nanoscale organised hierarchical composite tissue. In this application, the biomaterial must withstand significant mechanical forces generated in the tissue and promote osteogenic cell behaviour.

A widely investigated biomaterial is the synthetic polymer, polycaprolactone (PCL), which has been used for bone tissue engineering applications and *in vivo* is degradable, bioresorbable, and biocompatible

* Corresponding authors.
E-mail addresses: cian.vyas@manchester.ac.uk (C. Vyas), paulojorge.dasilvabartolo@manchester.ac.uk (P. Bartolo).
[1] Equal contribution.

https://doi.org/10.1016/j.msec.2020.111433
Received 30 April 2020; Received in revised form 19 August 2020; Accepted 21 August 2020
Available online 25 August 2020

[9,10]. These properties can be readily exploited in tissue engineering applications because PCL can easily be processed as it has a low melting temperature (~60 °C), soluble in a range of solvents (*e.g.* chloroform, dichloromethane, toluene, and acetone), excellent blending compatibility, and suitable rheological and viscoelastic properties enabling the fabrication of a variety of scaffolds using both conventional and additive manufacturing techniques [9–11].

Despite these advantages, PCL has a degradation profile that can be too long to match the formation and ingrowth of neotissue – it can take up to 4 years to degrade; depending on structural properties (*e.g.* thickness, porosity, and quantity), molecular weight, and the biological environment [9,12–15]. Furthermore, the biomechanical properties of PCL scaffolds are not appropriate for load bearing applications such as in bone tissue engineering and orthopaedics. PCL, in common with other synthetic polymers, also lacks biological cues and binding motifs to promote cell adhesion and modulate cell behaviour whilst the hydrophobic chemistry reduces cell attachment and spreading.

Subsequently, strategies to improve the degradation, mechanical, and bioactivity properties of PCL scaffolds are required. The mechanical properties can be improved through blending with both synthetic and natural polymers and the incorporation of particulate fillers such as bioceramics and carbon nanomaterials [16–18]. The functionalisation of specific chemistries and biological motifs onto the scaffold surface can enhance the bioactivity of scaffolds [19]. Whilst incorporating bioactive biomaterials such as collagen, gelatine, hydroxyapatite, tricalcium phosphate, and bioactive glass can promote cell attachment, proliferation, and differentiation down specific cell lineages [16,20–22]. For example, the development of a composite scaffold containing poly(L-lactic-*co*-ε-caprolactone), bovine bone matrix, and gelatin promoted faster and mature bone regeneration in human patients [23,24]. This demonstrates that the biological properties of PCL can be improved through the incorporation of the appropriate biological motifs.

The aim of this study is to address the challenges inherent to PCL of mechanics, degradability, and bioactivity by using silk as the material filler in the form of silk microparticles (SMPs). Silk is a protein-based natural polymer fibre, primarily composed of fibroin (core) and sericin (coating), which is biocompatible, biodegradable, and has excellent mechanical properties [25–28]. It has been used in Food and Drug Administration (FDA) approved medical devices such as sutures and has been investigated as a scaffold for tissue engineering applications [25–28]. In the three-dimensional (3D) bioprinting space, silk has predominantly been used as dissolved silk fibroin solution to produce hydrogel bioinks [29–31]. However, the dissolution process is time consuming and requires toxic chemicals. The production of silk particles directly through mechanical cutting and milling overcomes these issues. Moreover, the particles retain the natural microstructure of silk. SMPs and fibres have successfully been used as filler agents to enhance the mechanical and biological properties of scaffolds [32–37]. A rigid particle filler in a polymeric matrix can improve the compressive modulus, creep resistance, and fracture toughness of the composite [38,39]. Rajkhowa et al. demonstrated a 40-fold increase in compressive modulus and yield strength of a porogen leached silk scaffold reinforced with SMPs [40]. Furthermore, Mandal et al. [36] used alkali-hydrolysed silk microfibres as a filler in a silk scaffold whilst Gupta et al. [37] used chopped silk fibres to reinforce a lyophilised silk and hydroxyapatite coated scaffold which showed a 5-fold increase in compressive modulus. Additionally, Zhang et al. used SMPs, microfibres, and nanofibres to reinforce a 3D printed chitosan hydrogel which showed a 5-fold increase in compressive modulus and aided in printing fidelity and stability of the structure whilst maintaining biocompatibility [32,33]. Subsequently, the development of a PCL and SMP composite scaffold may improve the physical and biological properties of a scaffold for tissue engineering applications. The use of SMPs as a filler provides an alternative to other explored filler materials such as graphene, carbon nanotubes, hydroxyapatite, and bioglass which have been investigated to modulate mechanical and biological properties [16–18,22]. SMPs are biodegradable thus pose less of a cytotoxic and inflammatory risk compared to the use of graphene and carbon nanotubes whilst still providing an improvement to mechanical performance. Furthermore, silk has been shown to promote mineralisation and osteogenic behaviour in scaffolds thus can be utilised in a similar strategy as the inclusion, for example, of hydroxyapatite and bioglass [37,41–46]. Subsequently, a PCL/SMP composite scaffold can be used by itself or in combination with co-printing of hydrogels, containing SMPs, for bone tissue engineering applications [32,33,47].

Screw-assisted extrusion-based 3D printing was utilised in this study to produce PCL based scaffolds. This technique has previously been used to produce scaffolds for tissue engineering applications with homogenous and high particle loadings [16,48]. Furthermore, this process offers simplicity in use, lower cost to competing technologies, applicability to a wide range of materials including highly filled particle composites, and can be combined with multiple extrusion heads to fabricate multi-material scaffolds including the printing of cells. Alternative technologies such as selective laser sintering (SLS) have been employed to fabricate complex porous PCL scaffolds without the use of support structures [49,50]. However, they typically have partially melted structures which can limit their mechanical properties and the partially melted or loose powder potentially poses inflammatory risks, although thermal post-processing steps can minimise these issues [49]. SLS also cannot be easily used to generate multi-material scaffolds with distinct material regions, furthermore, cells are not able to be included in the printing process. Subsequently, the use of extrusion processes using polymer melts or solutions offers a simpler and widely accessible approach but may require support structures for complex structures.

This study presents a composite 3D printed PCL scaffold reinforced with SMPs to improve the mechanical, biological, and degradation properties. The rheological and thermal properties of the PCL/SMP composites with different particle loadings were evaluated. The scaffolds were fabricated using a screw-assisted melt extrusion 3D printing system and scaffold morphology was characterised using scanning electron microscopy and micro-computed tomography. The effect of SMP loading on the surface roughness, mechanical properties, wettability, protein adsorption, and *in vitro* enzymatic degradation of the scaffolds was assessed. Finally, human adipose derived stem cells were used to assess the *in vitro* biological properties of the scaffold with cell metabolic activity, viability, and morphology evaluated.

2. Materials and methods

2.1. Materials

Bombyx mori silk fibres (Automatic Silk Reeling Unit, Ramanagaram, India) which was reeled and undegummed was processed using a previously reported protocol [51]. The silk was degummed using a rotary textile dyeing machine (Ahiba IR Pro, Datacolor, USA) for 30 min at 98 °C in a 2 g/L sodium carbonate (Sigma-Aldrich, USA) and 1 g/L olive oil soap (Vasse Virgin, Australia) solution, with a material mass (g) to solution volume (mL) ratio of 1:50. The degummed silk fibres were washed three times each in tap water then deionised water to ensure the removal of all chemical traces. Finally, the silk fibres were dried overnight at 40 °C. The SMPs were produced using a physical milling process previously reported that consists of a combination of chopping, wet milling and spray drying [52]. PCL (M_w = 50,000 Da, CAPA 6500, Perstorp, UK) in the form of 3 mm pellets was used as the polymer matrix.

PCL/SMP composites were prepared through melt blending. PCL pellets were melted at a temperature above 80 °C and then SMPs were added to the PCL melt to achieve the desired particle loadings of 10 wt %, 20 wt%, and 30 wt% SMPs. The mixtures were physically blended for at least 15 min to ensure a homogeneous dispersion of silk powder. Finally, the prepared blends were cooled and cut into smaller pieces

ready for scaffold fabrication and experimental testing.

2.2. Particle characterisation

The SMP morphology was assessed by scanning electron microscopy (SEM) and laser diffraction particle size analyser.

The particles were sputter coated with platinum for 60 s obtaining a ~10 nm coating and then imaged with SEM (S-3000N, Hitachi, Japan) with an accelerating voltage of 10 kV. The particle morphology was assessed using the open source software Fiji.

A laser diffraction particle size analyser (Mastersizer 3000, Malvern Panalytical, UK) was used to quantify the particle size and volume distribution. The SMPs were dispersed in water (refractive index = 1.33) and the particle refractive index was 1.561. A Mie scattering and a general-purpose analysis model was used. Sonication was employed prior to measurement to reduce bubble formation and disperse any agglomerates. Five measurements of the dispersed SMPs were performed.

2.3. Rheology

The rheological properties of PCL/SMP composites were measured using a dynamic rotational rheometer (HR-3 Rheometer, TA Instruments, USA). Due to the difficulty in obtaining high shear rates with a polymer melt in a rotational rheometer the Cox-Merz rule was used to correlate the dynamic oscillatory low-shear data obtained with high-shear viscosity, generating the complex viscosity (η*) [53].

Samples were prepared by melt-blending into a disc shape of 15 mm diameter and 1 mm thick. Oscillation testing was implemented using a parallel plate geometry (plate diameter 40 mm), geometry gap of 1 mm, and temperature of 140 °C. Amplitude sweep measurements with a strain value of 10^{-1} to 10^{2}%, frequency kept constant at 1 Hz, were performed in advance to ensure the selected strain value was within the linear viscoelastic range (LVR). A 1% strain value was then chosen for the dynamic frequency sweep tests with a frequency range of 0.1 to 100 Hz.

2.4. Thermal analysis

Thermal analysis of PCL and PCL/SMP scaffolds was performed using differential scanning calorimetry (DSC, Q100, TA Instruments, USA) with a nitrogen atmosphere. An indium standard was used to calibrate the heat enthalpy and temperature of the DSC. Each sample (n = 3) of ~5 mg was placed in an aluminium pan for the measurement. All specimens were heated to 70 °C at a rate of 10 °C/min from the ambient temperature to erase the previous thermal history. This was followed by cooling to −30 °C and reheating up to 70 °C at a rate of 10 °C/min to evaluate the thermal properties including melting behaviour and crystallisation. The following equation was used to calculate the degree of crystallinity (X_c) (54):

$$\mathrm{Xc}\,(\%) = \frac{\Delta \mathrm{Hm}}{\varphi.\ \Delta \mathrm{Hm}*} \times 100\% \quad (1)$$

where ΔH_m refers to the melting enthalpy from the second heating curves, φ, is the weight fraction of PCL in the composites, and ΔH_m* is the melting enthalpy of the polymer with complete crystallisation, for PCL was reported to be 142 J/g [55].

2.5. Scaffold fabrication

Scaffolds were fabricated using a screw-assisted extrusion-based additive manufacturing system (3D Discovery, RegenHU, Switzerland). The scaffolds were designed with a 0°/90° lay-down pattern, 300 μm fibre diameter, 300 μm pore size, and 255 μm layer-thickness. The material and screw chamber temperature were kept constant at 140 °C and 90 °C, respectively, and an air pressure of 6 bar was supplied to the material chamber. Qualitative observation showed that a higher material chamber temperature was required to allow continuous movement of material into the screw chamber, thus the temperature was raised to 140 °C to enable this. The screw rate was kept constant at 7.5 rpm for all material compositions, however, the feed rate was varied to obtain an appropriate fibre diameter, due to changes in viscosity of the composites, which was assessed using an optical microscope (VHX-5000, Keyence, Japan). Subsequently, a feed rate of 11.75, 12.75, 13.25, and 13.75 mm/s was selected for PCL, 10 wt%, 20 wt%, and 30 wt% SMPs, respectively. Higher percentage SMP loadings, 40 wt%, was attempted. However, the high particle filler content resulted in repeated blocking of the extrusion nozzle. Furthermore, the increase in viscosity required a significant increase in temperature (200 °C) to maintain material flow which potentially can cause material degradation. The printed scaffolds were 40 mm × 40 mm × 2.5 mm with a one-layer thick brim around the perimeter to provide adhesion to the print platform. Scaffolds were cut to 6.5 mm × 6.5 mm × 2.5 mm, a calliper was used for quality control, for experimental studies.

2.6. Scaffold characterisation

2.6.1. Scaffold morphology

Scaffold morphology was assessed through SEM and micro computed X-ray tomography (μCT).

The scaffolds for SEM (S-3000N, Hitachi, Japan) were sputter coated for 60 s with platinum to obtain ~10 nm coating and imaged with an accelerating voltage of 10 kV. Top-down and cross-sectional images were obtained. Energy dispersive X-ray spectroscopy (EDX; Oxford Instruments, UK) was used to investigate the elemental composition of the scaffold surface after *in vitro* cell culture.

Three-dimensional imaging was obtained using μCT (SkyScan 1172, Bruker-microCT, Kontich, Belgium). Scanning parameters were set to 9 μm pixel size, X-ray source with 100 kV and 100 mA and using no filters. Samples were rotated 360° around their vertical axis with a rotational step of 0.4 degrees. The images were reconstructed using the software (NRecon, Bruker-microCT, Kontich, Belgium) and subsequently analysed with another software (CTAn, Bruker-microCT, Kontich, Belgium) which allowed for quantitative analysis of the scaffolds morphological parameters such as porosity, pore size, fibre diameter, and surface to volume ratio. Interconnectivity was calculated with an algorithm, as previously described, by considering only the open and accessible pore volume within the scaffold [56,57].

2.6.2. Surface topography

The surface roughness (S_a) of the scaffolds (n = 3) was assessed through optical profilometry using a laser scanning digital microscope (LEXT OLS4100, Olympus, Japan) at ×50 magnification on an individual fibre with a scanning area of 257 × 258 μm. The areal scanning method was used to measure a specific area of the surface to obtain the mean surface roughness, S_a, which is a 3D parameter of the arithmetic mean roughness obtained from the 2D parameter (R_a).

2.7. Mechanical assessment

2.7.1. Bulk mechanical properties

Uniaxial compression using a universal testing machine (INSTRON 4507, UK) was used to assess the bulk mechanical properties of the scaffold and the role of SMPs in reinforcing the PCL matrix. The samples (n = 5) in the dry state were compressed at strain rate of 0.5 mm/min with a 2 kN load cell up to a strain of 40%. The compressive Young's modulus was calculated from the gradient of the linear elastic region. The compressive strength at 1, 10, and 40% strain and the yield strength (using 2% strain offset method, typical of polymeric materials) are reported (Fig. S1 - supplementary information).

2.7.2. Nanoindentation

The nanomechanical properties of the PCL/SMP scaffolds were characterised using nanoindentation (Hysitron TI 950 Tribo-Indenter, Bruker, USA). The equipment was fitted with a standard three-sided pyramidal (Berkovich) probe and the probe area (A) function was calibrated independently before the test. A 50 μm spacing was used between indents with 10 indents for each sample.

Samples were mounted in epoxy and polished down to a 40 nm surface finish. The indenter was forced into the sample at 400 μN/s for 5 s, held at a peak load of 2000 μN (P_{max}) for 2 s and unloaded at 400 μN/s. The force and displacement were recorded for the entire duration of the test. The nanoindenter data analysis software (Hysitron TI 950 Tribo-Indenter, Bruker, USA) was used to estimate hardness (H). The software uses, P_{max} and A for hardness estimation.

$$H = \frac{P_{max}}{A} \tag{2}$$

where P_{max} is 2000 μN and A is the contact area [58].

The unloading segments of each indentation was analysed using the data analysis software which follows the Oliver-Pharr model [59] to fit the initial unloading portion (95%–80%) of the force-displacement curve and extracts the Reduced Modulus (E_r).

$$E_r = \frac{S\sqrt{\pi}}{2\sqrt{A}} \tag{3}$$

where S is the contact stiffness and A is the projected contact area [59].

2.8. In vitro enzymatic degradation

The degradation properties of the PCL and PCL/SMP scaffolds were assessed using a model accelerated *in vitro* enzymatic degradation method based on previous studies with slight modification [51,55]. All samples were first conditioned to 20 °C ± 2 °C and 65% ± 2% relative humidity for at least 48 h. The weight of each sample was then recorded before sterilisation by 30 min of ultraviolet (UV) irradiation. Control samples ($n = 3$) were immersed in 1 mL of 0.1 M phosphate buffered saline (PBS) at pH 7.4 solution in a 24-well plate. Experimental samples (n = 3) were placed in a solution of 1 mL of 0.1 M PBS containing 0.5 mg/mL of lipase from *Thermomyces lanuginosus* (Novo Nordisk, Copenhagen, Denmark). Samples were then incubated in a standard cell culture incubator (5% CO_2, 37 °C, and 95% humidity) and removed after 6, 12, 24, 48, and 96 h. During the incubation, the lipase and PBS solution were changed every day to ensure enzyme activity.

At each time point, samples were removed and rinsed with deionised water three times and dried in a fume hood overnight. The dried samples were then conditioned again to 20 °C ± 2 °C and 65% ± 2% relative humidity for at least 48 h and re-weighed. The weight loss of each sample was expressed as a percentage of the original weight. The scaffold mass was considered zero when the scaffold structure itself was degraded and only pieces remained. The scaffold surface morphology was evaluated qualitatively during the degradation process using laser scanning digital microscopy (LEXT OLS4100, Olympus, Japan) at each time point.

2.9. Wettability

The wettability of the scaffolds was determined through a static water contact angle measurement (KSV Cam 200, Finland). Images were obtained immediately after droplet formation on the scaffold ($n = 3$) and analysed using the Sessile drop technique.

2.10. Protein adsorption

Fetal bovine serum (FBS) was used as a model protein system to quantify the amount of protein that would adsorb onto the scaffolds. The bicinchoninic acid assay (BCA) (Micro BCA Protein Assay Kit, Thermo Fisher Scientific, USA) was used following the manufacturer's instructions and experimental procedure based on previously reported studies [60]. Briefly, the scaffolds ($n = 3$) were pre-wet using a PBS solution in an incubator (5% CO_2, 37 °C, and 95% humidity) overnight. The samples were then immersed in a 10% FBS solution and kept in the incubator for 12 h. The scaffolds were then gently washed in PBS to remove excess and unattached protein. Samples were moved to a new plate to guarantee that only protein adsorbed to the scaffolds was quantified and the working reagent was added. After 2 h of incubation (5% CO_2, 37 °C, and 95% humidity), 150 μL from each sample was transferred to a 96-well plate and read at an absorbance of 562 nm using a microplate reader (Infinite 200, Tecan, Switzerland). The amount of protein absorbed was calculated according to a standard curve generated by a dilution series of bovine serum albumin (BSA) standards and normalised to non-protein treated samples ($n = 3$).

2.11. Biological assessment

2.11.1. Cell culture and seeding

The printed scaffolds were washed twice in sterile PBS, sterilised by immersion in 80% ethanol for 2 h, washed again twice with sterile PBS, and then dried overnight in a sterile tissue culture laminar flow cabinet ready for cell seeding.

Human adipose derived stem cells (hADSCs, STEMPRO™, Thermo Fisher Scientific, USA) were used for *in vitro* biological assessment of the scaffolds. hADSCs were maintained and expanded in MesenPRO RS™ media containing 2% (v/v) growth supplement, 1% (v/v) glutamine, and 1% (v/v) penicillin/streptomycin, and incubated using standard conditions (5% CO_2, 37 °C, and 95% humidity). The culture medium was changed every three days. Cells were harvested at passage 7 and at ~80% confluency using a 0.05% trypsin-EDTA solution (Sigma-Aldrich, USA). A cell suspension was prepared (0.33×10^6/mL) and 25,000 cells in 75 μL of media were statically seeded onto each scaffold. The solution was pipetted on top of the scaffold in a non-treated 48-well plate and incubated in a standard cell culture incubator for 2 h to allow cell attachment, before the addition of 325 μL fresh media supplement. The cell culture media was changed every three days. Non-treated well plates were used to minimise cell migration and attachment to the underlying tissue culture plastic (TCP), as proposed by Sobral et al. [61]. All cell seeded scaffolds were transferred to a new 48-well plate on day 1.

2.11.2. Cell metabolic activity

Cell metabolic activity was assessed at day 1, 3, 7, 14, and 21 after cell seeding, using the resazurin assay (Sigma-Aldrich, UK), commonly referred to as Alamar Blue, which functions by the reduction of resazurin to resorufin by metabolically active cells. This assay can provide an indication of cell proliferation. On day 1 all samples ($n = 12$) were transferred to a new 48-well plate to enable quantification of cell attachment and prevent unattached cells from influencing the result. TCP was used as a positive control, non-seeded scaffolds as a negative control, and media as a blank. At each time point, a 10% by volume (40 μL) of resazurin solution (0.01% (v/v)) was added to each sample and incubated for 4 h. After incubation, 150 μL of each sample was transferred to a 96-well plate and the fluorescence intensity was measured (540 nm excitation/590 nm emission wavelength) with a plate reader (infinite 200, Tecan, Switzerland). Samples were washed twice in sterile PBS to remove the resazurin solution before the addition of fresh media.

2.11.3. Cell viability

Cell viability was assessed using a Live/Dead assay kit (ThermoFisher Scientific, UK) at day 21 according to the manufacturer's instructions. Culture media was removed from the samples and TCP control and washed twice with PBS before adding 500 μL of a calcein-

AM (2 μM) and ethidium homodimer-1 (EthD-1, 4 μM), PBS solution. Ethanol treated TCP samples were used as EthD-1 positive controls (dead). The samples were then incubated for 25 min in an incubator. Scaffolds were imaged with an inverted fluorescence microscope (Leica DMI6000 B, Leica Microsystems, Germany). Day 1 imaging was attempted, however, the EthD-1 would bind to the SMPs giving rise to false positives in the dead channel (Fig. S2 - supplementary information).

2.11.4. Cell morphology

Cell attachment and morphology on the scaffolds was imaged using SEM (Hitachi S-3000 N, Hitachi, Japan) on day 7, 14, and 21. Scaffolds were gently washed twice with PBS and then fixed with 2.5% glutaraldehyde solution for 1 h. After fixation, scaffolds were washed with PBS twice, followed by dehydration in a sequential series of ethanol concentrations (50, 60, 70, 80, 90, and 100%) for 15 min at each concentration with the 100% ethanol concentration repeated. Hexamethyldisilazane (HMDS, Sigma-Aldrich, UK) and ethanol in a 50:50 mixture was then used to treat scaffolds for 15 min. Finally, a 100% HMDS solution was used and the samples were then left to dry for 24 h in a fume cupboard to allow the HMDS to evaporate before platinum coating and SEM imaging.

2.12. Statistical analysis

Statistical analysis was performed using one-way analysis of variance (ANOVA) and multiple comparisons with Tukey *post-hoc* test using GraphPad Prism software (Graphpad Software Inc., USA) and all values are reported as mean ± standard deviation (SD). The differences between means were considered significant at $*p < 0.05$, $**p < 0.01$, $***p < 0.001$ and $****p < 0.0001$.

3. Results and discussion

3.1. Silk microparticle morphology

The SMPs were characterised by a laser diffraction particle size analyser and SEM to determine particle morphology (Fig. 1). The particles have an irregular shape with a spherical cauliflower-like morphology and an equivalent sphere diameter of ~6–7 μm and 90% of the particles sized below ~10 μm. The particle volume distribution is relatively narrow with only a single peak, which demonstrates that the SMP fabrication process produces uniform particles.

3.2. Composite rheology

The PCL/SMP composites were analysed to assess the impact of SMPs on the rheological behaviour of the polymer matrix (Fig. 2). The rheological results were reproducible even after repeated melt-cooling rheology measurements, which indicated good stability and dispersion of the SMPs within the PCL matrix with no additional crystal alignment or degradation induced by the temperature cycling [62]. The storage (G′) and loss (G″) modulus of PCL and PCL/SMP blends all showed liquid-like behaviour with G″ higher than G′ at 140 °C, regardless of the SMP weight loading. As the SMP loading increased, from 10% to 30%, both G′ and G″ of the composites increased with the silk content, which agrees with previous studies on PCL-based nanocomposites filled with clay [63], starch-based nanoparticles [54], nano-hydroxyapatite and tricalcium phosphate particles [64]. The addition of SMPs caused a more pronounced effect on G′ than on G″, thus enhancing the elasticity, which is characterised as a pseudo-solid-like-response of the composite material [63].

The loss factor tan δ, which indicates the ratio of the loss modulus to storage modulus, as a function of frequency shows that the tan δ of pure PCL decreases with increasing frequency, indicating its viscoelastic liquid-like behaviour (Fig. 2b). At frequencies lower than 10 rad/s, there is a clear difference between PCL and PCL/SMP composites with the tan δ for pure PCL being much higher, indicating the evident elastic response introduced by the addition of SMPs with less energy being dissipated. As the silk content increases, the PCL polymer macromolecule motion is largely retarded by the presence of the SMPs and thus the polymer relaxation is slower at low frequencies [54]. At higher frequencies (> 10 rad/s) the tan δ of all samples converge and the materials exhibit an increasing elastic response as the difference between G' and G" decreases.

The complex viscosity (η*) as a function of frequency is dependent on the SMP content (Fig. 2c) As the SMP content increases the η* increases, which agrees with the change observed in the G′ and G″. The 30 wt% SMP composite showed the largest increase in η* compared to other samples, due to a more pronounced particle reinforcement in the polymer network structure. As the frequency increases a clear shear thinning behaviour is observed which is more prominent with increasing silk loading especially at 30 wt% SMP which has the largest decrease in η*. The change in viscosity is due to the structural reorganisation of the polymer network due to the introduction of the SMP filler which results in particle-particle and particle-polymer interactions. The shear thinning behaviour observed is typical of particle filled polymers and can be associated with the inter-particle distances being disturbed which results in reduced particle-particle interactions thus disrupting the initial 3D structure [65]. The particles are rearranged in the direction of flow with a layered structure forming within the matrix which is less resistant to flow, and the materials behave in a more non-Newtonian shear-thinning manner.

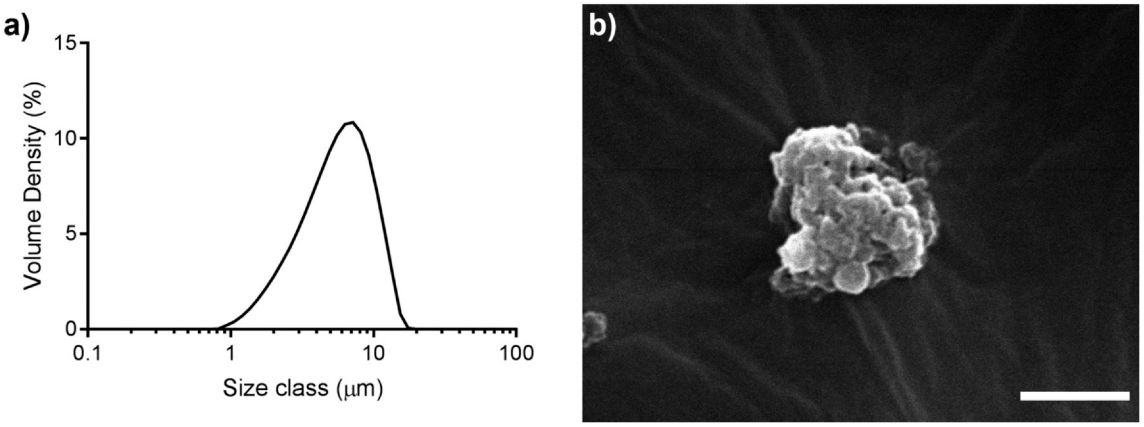

Fig. 1. Silk particle morphology. a) Particle volume distribution; Dx (10) = 2.39 μm ± 0.0228, Dx (50) = 5.72 μm ± 0.00953, Dx (90) = 10.6 μm ± 0.0582, and volume moment mean, D (4, 3) 6.14 μm ± 0.0067. b) Representative SEM image of the SMPs (scale = 5 μm).

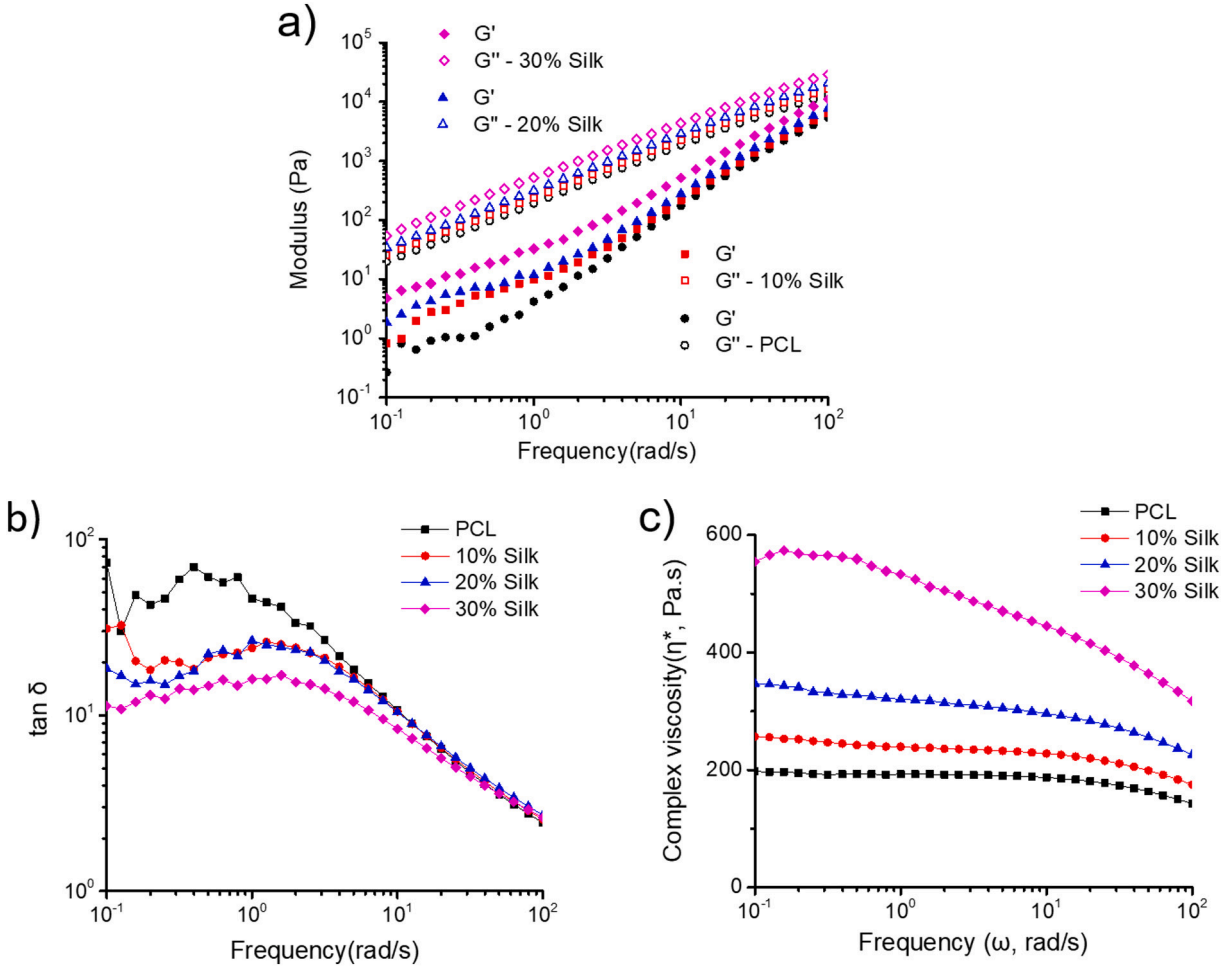

Fig. 2. Rheological properties of PCL and SMP composites. Frequency dependency of a) dynamic storage modulus (G′) and loss modulus (G″), b) tan δ, and c) complex viscosity (η*).

3.3. Thermal analysis

DSC was used to determine the thermal properties of the PCL/SMP composite with the cooling and subsequent heating curves allowing the determination of the crystallisation peak temperature (T_c), crystallisation enthalpy (ΔH_c), melting temperature (T_m), ΔH_m, and X_c (Fig. 3. and Table 1). The addition of SMPs led to an increased T_c with the increase independent of SMP loading. The pure PCL showed a crystallinity of 45.6%, similar to previous reported studies [54,66]. Increasing the SMP loading led to a decrease in ΔH_c and subsequently the X_c of the composite. The SMPs had limited influence on the T_m even with a decrease in the ΔH_m.

An increase in the crystallisation temperature after adding SMPs may indicate that the particles can act as heterogeneous nucleating agents and lower the nucleation free energy required for the PCL matrix, therefore resulting in higher T_c [54]. The decrease in crystallinity

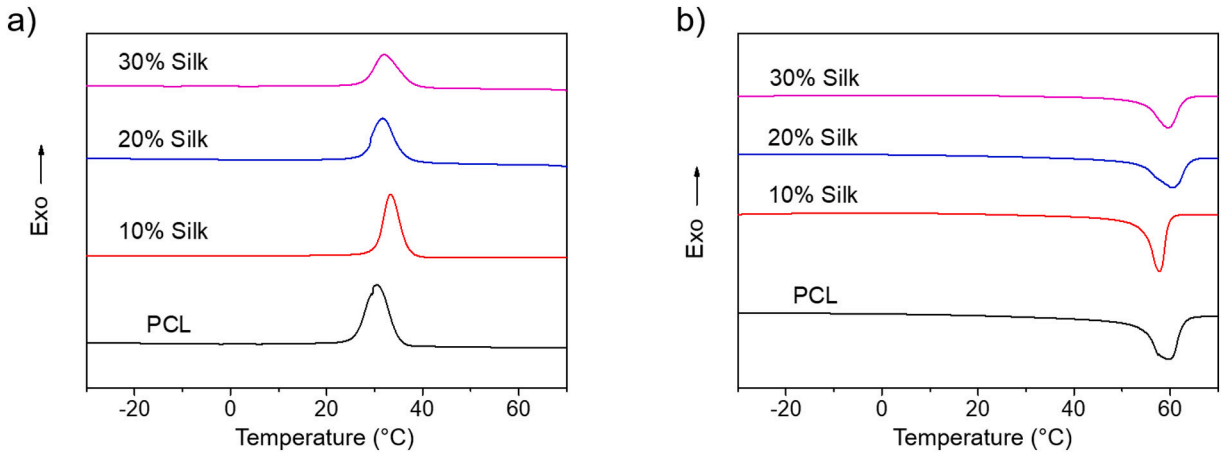

Fig. 3. DSC a) cooling and b) second heating curves of PCL/SMP composite scaffolds.

Table 1
DSC data of PCL/SMP composite scaffolds obtained from the cooling and the second heating DSC curves.

	T_c (°C)	ΔH_c (J/g)	T_m (°C)	ΔH_m (J/g)	X_c (%)
PCL	29.64	64.48	59.34	64.77	45.6
10% SMP	32.98	55.86	57.38	55.59	43.5
20% SMP	31.82	49.52	60.38	47.98	42.2
30% SMP	32.02	41.66	59.58	41.23	41.5

caused by the addition of SMPs suggests an interaction with the PCL matrix which disrupts crystal formation [67]. A similar reduction in matrix crystallinity has also been reported in other particle reinforcing studies such as nano-cellulose reinforced polyethylene oxide [68]. A decrease in the ΔH_m of the composite is most likely caused due to the increasing SMP content and less PCL per unit weight as the melting behaviour was not affected by SMP as only a small change in melting temperature was observed.

3.4. Scaffold morphology

The 3D printed scaffold morphologies were observed using SEM and μCT (Figs. 4 and 5). The SEM shows that the composite PCL/SMP scaffolds were successfully 3D printed. The scaffolds have a regular overall geometry with 0°90° architecture (log-pile) and the printed fibres and pores between them are clearly defined and uniform. The increasing loading of SMPs is clearly observed in the rougher surface of the printed fibres and particles embedded in the fibre cross-sections.

The scaffold dimensions closely matched the designed criteria of 300 μm for both fibre diameter and pore size. The scaffolds were designed with a 300 μm pore size as studies have demonstrated values in this region are suitable for bone tissue engineering applications, although the specific pore size is dependent on the final application [69–71]. The fibre diameter decreased with increasing loading of SMP with 30 wt% SMP having a diameter of 269.9 ± 5.0 μm compared to pure PCL of 301 ± 5.3 μm. As the fibre diameter decreased, with increasing loading of SMP, the resulting pore size increased (Fig. 5a). The total porosity was approximately 55% for all scaffolds. Scaffold interconnectivity was > 85% for all scaffolds at a pore threshold size of 200 μm and approaching 100% at smaller thresholds (Fig. 5b). Full morphological measurements can be observed in Table S1 in the supplementary information. This demonstrates excellent interconnectivity and a major advantage of using additive manufacturing for the fabrication of scaffolds. Pore interconnectivity is crucial to allow tissue ingrowth and diffusion of nutrients, gases, biomolecules, and waste removal throughout the scaffold [72–75]. The change in rheological

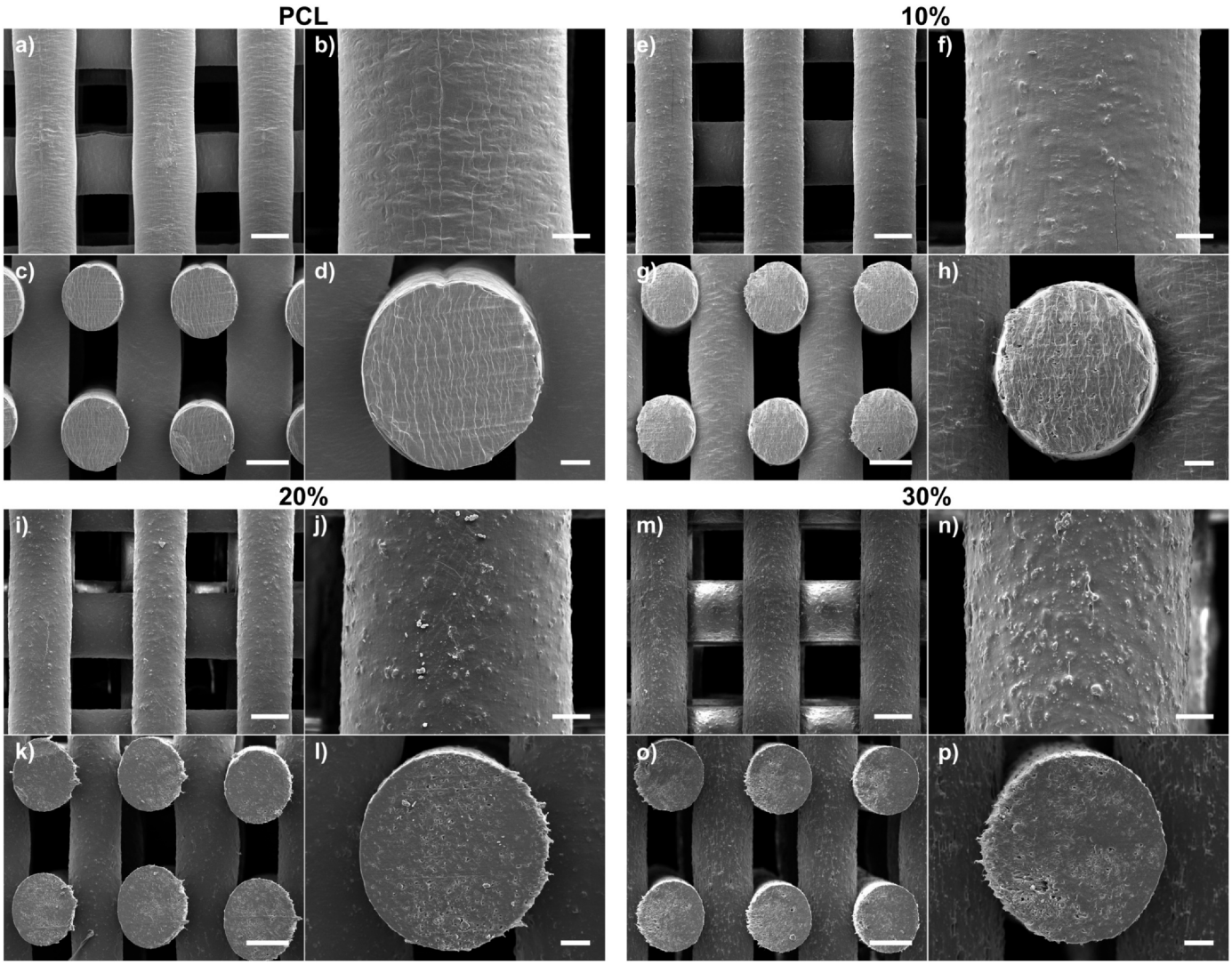

Fig. 4. Scanning electron microscopy images showing: a, e, i, m) top view (scale = 200 μm); b, f, j, n) fibre surface (scale = 50 μm); c, g, k, o) cross-section (scale = 200 μm); and d, h, l, p) fibre cross-section (scale = 50 μm) of the 3D printed PCL/SMP scaffolds.

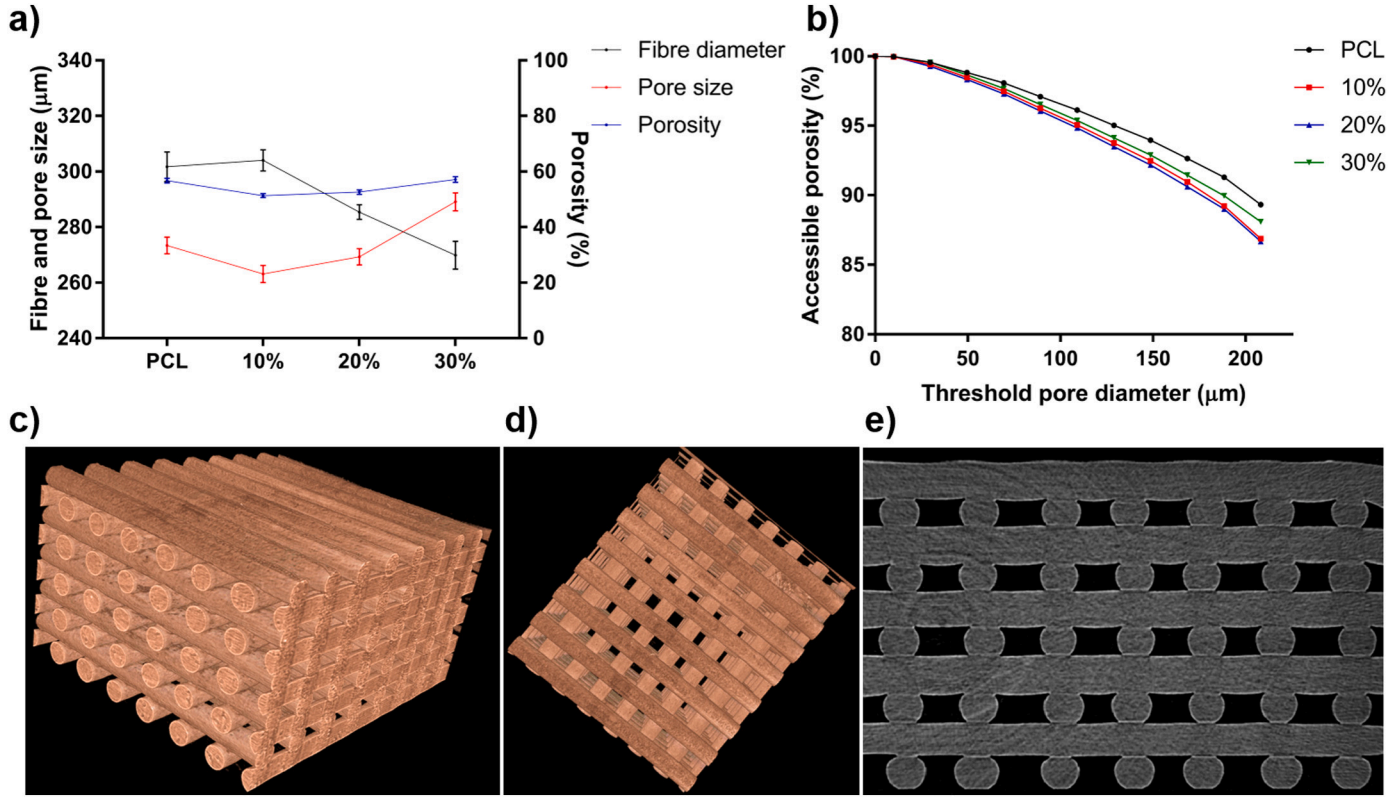

Fig. 5. μCT X-ray tomography imaging and analysis of the 3D printed PCL/SMP scaffolds. a) Fibre diameter, pore size, and porosity of the scaffolds. b) Accessible porosity of the scaffold as a function of pore diameter threshold. c) and d) μCT reconstructions of the scaffold. e) Cross-section of the PCL scaffold.

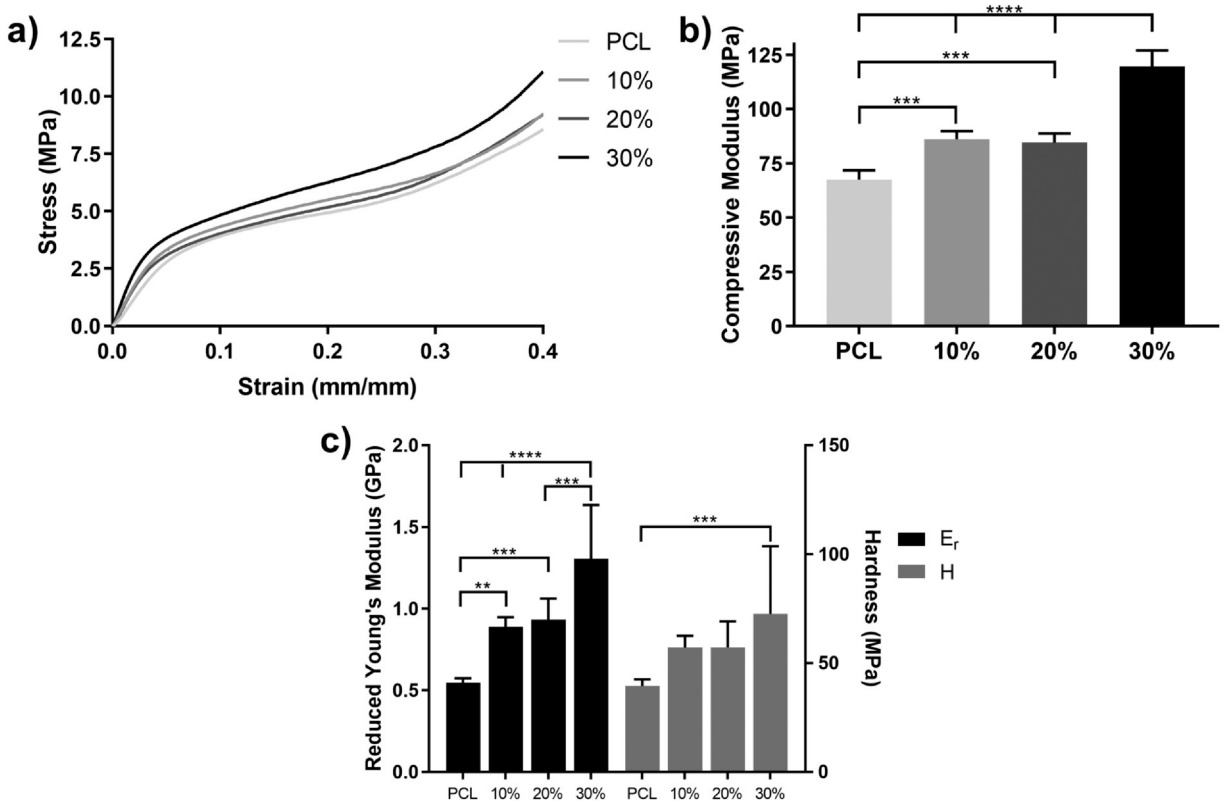

Fig. 6. Bulk and nano mechanical properties of the PCL/SMP scaffolds. a) Representative bulk compression stress-strain curves of the scaffolds. b) Compressive Young's modulus of the scaffolds. c) Reduced Young's modulus and hardness determined through nanoindentation.

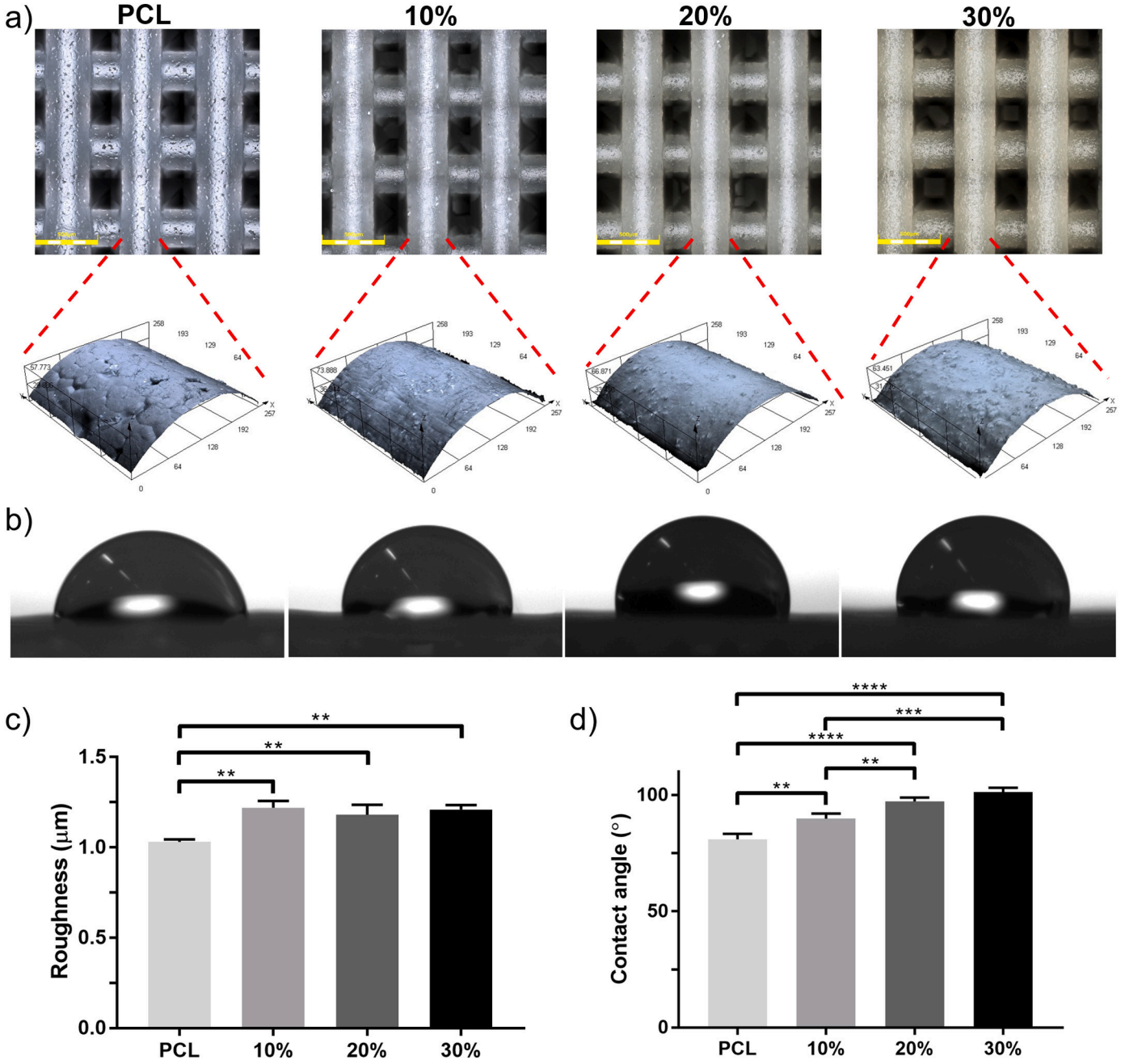

Fig. 7. Surface roughness and wettability of the PCL/SMP scaffolds. a) Laser microscopy 3D topographic reconstruction of the scaffolds and high magnification of the fibre surface (scaffold reconstruction: scale = 500 μm and fibre surface: scan size = 257 × 258 μm). b) Water droplet profiles on the scaffold surface. c) Surface mean roughness, S_a, and d) water contact angle measurements of the scaffolds.

behaviour of the composite material affects material flow thus the fibre dimension. Although the printing process has been optimised; the small changes in dimensions throughout a scaffold are not immediately obvious from SEM characterisation but is clear when using μCT which allows the entire structure to be measured. Additionally, some fibre delamination can be observed at 30 wt% SMP loading which is not observed on the other scaffolds but is related to differences in actual fibre dimension to the design dimensions (Fig. S3 – supplementary information). Further optimisation is required of the 3D printing process parameters to reach the desired design criteria.

Finally, no information can be determined about the SMP distribution within the PCL matrix using μCT as the absorption contrast was not sufficient to segment the SMPs from the PCL. However, the SMPs are assumed to be homogenous within the PCL due to the thorough physical blending process and then mixing within the screw-chamber in the extruder during printing. Furthermore, the interfacial surface energy in the PCL/SMP system will play a critical role in their dispersion, the spherical shape of the SMPs is likely to assist in dispersion due to the lower surface area compared to particles with a flaky morphology that can tend to aggregate [76]. The SEM images show an apparent homogenous distribution on the fibre surface and cross-section (Fig. 4).

3.5. Mechanical properties

The bulk and nano mechanical properties of the PCL/SMP scaffolds were evaluated using uniaxial compression testing and nanoindentation, respectively. The bulk mechanical properties are important, as

they need to match the intended tissue and withstand physiological forces imposed on the structure, especially in load bearing applications such as bone and cartilage. The nanomechanical properties influence cell behaviour through mechanotransduction pathways as the cells sense the biophysical environment [77–79]. Thus, both should be designed for the intended application.

The PCL/SMP scaffolds show typical behaviour of a cellular solid with the stress-strain profiles showing an initial linear elastic behaviour, plateau phase, and then a densification region (Fig. 6a) [80]. The bulk compressive modulus significantly increased with increasing loading of SMPs from 67.51 ± 4.25 MPa to 119.70 ± 7.34 MPa for PCL and 30 wt% SMP, respectively (Fig. 6b). Although the compressive modulus of cortical bone is considerably higher (7–18 GPa), the 30 wt% SMP scaffold is within the lower region of trabecular bone (0.1–5 GPa) [81]. The difference between 10 wt% and 20 wt% SMPs scaffolds is minimal and not statistically significant. This may have arisen due to the differences in scaffold morphology with the 20 wt% SMP scaffolds having a smaller fibre dimeter and larger pore size than the 10 wt% SMP scaffolds, thus the 3D printing process parameters requires further optimisation, as previously stated. Subsequently, the mechanical properties may not follow a proportional relationship with particle filler loading.

The nanomechanical properties also increase with loading of SMPs into the PCL matrix (Fig. 6c). The reduced Young's modulus significantly increases from 0.55 ± 0.03 GPa to 1.31 ± 0.33 GPa for PCL and 30 wt% SMP, respectively. The stiffness of the scaffold surface significantly increases with inclusion of SMPs and stiffer surfaces promote osteogenic differentiation; a surface elasticity of ~40 kPa promotes osteogenic behaviour, thus the stiffness of the PCL/SMP composite is considerably higher [79]. However, the elastic modulus of trabecular bone observed through nanoindentation is higher (> 7 GPa) [82,83]. The hardness also significantly increases with SMP loading with the moduli increasing from 39.47 ± 3.08 MPa to 72.64 ± 30.96 MPa for PCL and 30 wt% SMP, respectively. However, these values are lower than the hardness observed in trabecular bone (~500 MPa) [83]. A similar nanomechanical behaviour is observed between 10 wt% and 20 wt% SMPs scaffolds which agrees with the observation for the bulk mechanical properties. However, this may be related to the quantity of SMPs present at the fibre surface influencing these nanomechanical properties. As qualitative observation of the fibre surface shows similar quantity of SMPs between 10 wt% and 20 wt. SMP scaffolds but a large increase at 30 wt% (Fig. 4n). A threshold may be reached at 30 wt% which influences particle packing, distribution volume, and particle-polymer interactions. This can be observed through the previous rheological and thermal analysis which shows a clear trend related to increasing SMP content with 30 wt% having a distinct behaviour, especially rheological. This particle threshold behaviour may be responsible for the nanomechanical and in addition, the bulk mechanics observed.

The inclusion of SMPs as a reinforcing agent within the PCL matrix provides a significant increase to both the bulk and nanomechanical properties of the scaffold compared to PCL alone. Further investigation is required to elucidate the influence of SMPs on the PCL matrix and subsequent bulk and nanomechanical properties.

3.6. Surface roughness and wettability

The surface topography and wettability of the 3D printed PCL/SMP scaffolds were determined through laser microscopy and water contact angle measurement, respectively (Fig. 7). Biomaterial surface topography and wettability are important as they influence protein adsorption and cell-material interactions [19,84–86]. The characterisation and engineering of the surface properties will enable the facilitation of specific cell behaviour.

Laser microscopy demonstrated that all 3D printed scaffolds had good print quality, with well-defined fibres and uniform pore distribution, complimenting the SEM and μCT imaging. The surface morphology of the pure PCL scaffolds shows hexagonal surface features and a considerable number of hollow voids or pits clearly observable (Fig. 7a). These features can be attributed to crystalline microstructure formation and the rheological behaviour during extrusion and the subsequent cooling resulting in the observable hexagonal and pitted surface features [65,87,88]. The hollow pitted surface of the scaffold fibres disappeared with the addition of SMPs as the crystallisation kinetics and rheology were altered, as previously demonstrated in the DSC and rheological analysis. The fibre surface morphology is sensitive to changes in rheology as demonstrated by Huang et al. in a 3D printed PCL scaffold including multi-walled carbon nanotubes which resulted in a 'sharkskin' effect on the fibre surface [17]. The inclusion of SMPs did not alter the overall fibre morphology, remained circular and non-wavy, but became significantly rougher due to the presence of microparticles and altered the colouration of the scaffolds.

The addition of SMPs into the PCL scaffolds resulted in a colour change from white to a yellowish tinge throughout, which increased with higher silk loading (Figs. 7a and S4 – supplementary information). The cause of the yellowing is unclear, whilst the microparticles themselves do have an off-white yellowish colour, the scaffolds printed with high SMP content were considerably more yellow than the original particles [52]. There could be a degree of thermal degradation of the silk due to the high temperature used during the printing process, however, thermal analysis shows that the printing temperature of 140 °C is considerably lower than the degradation temperature of silk particles, approximately 300 °C [33]. Another possible cause may be thermal oxidation of some of the side chains in fibroin. Four major amino acid residues in the silk fibroin chain (glycine, alanine, serine and tyrosine) can be involved in thermal oxidation reactions, with the reaction products producing pigmented phenolic groups that contribute to the colour development. Nevertheless, high temperature printing could lead to instability in the SMPs due to oxidation reactions, thus, further investigation of SMP stability is required. Therefore, printing in an inert environment or at lower temperatures might be considered in the future to avoid any potential degradation effects.

The PCL/SMP scaffold surface roughness, S_a, increased with larger SMP loading (Fig. 7c). The S_a of the pure PCL scaffolds was 1.03 ± 0.01 μm; the SMP containing scaffolds had a significantly higher S_a of up to 1.22 ± 0.04 μm, at 30 wt% SMP. There was no significant difference between SMP containing scaffolds, the size and distribution of the SMPs appeared to be homogeneous within the PCL matrix, thus resulting in a similar mean surface roughness regardless of SMP loading.

The wettability of a biomaterial surface is dependent on surface chemistry and roughness with hydrophilic surfaces having a water contact angle less than 90° whilst above this value the material becomes hydrophobic. The wettability of the PCL/SMP decreased (hydrophobicity increased) with increasing SMP content with the contact angle significantly increasing from ~80° to ~100° for PCL and PCL/SMP 30 wt%, respectively (Fig. 7b and d). PCL is an inherently hydrophobic polymer with typically a contact angle above 90°, the lower value in this study can be attributed to the large pores in the printed structure which allows the droplet to seep into the structure [9]. The increase in hydrophobicity with increasing SMP content can be attributed to two parameters: the increase in surface roughness and the highly crystalline content of SMPs. As observed by laser microscopy the surface roughness increases with increasing SMP content. As PCL is inherently hydrophobic the increase in roughness will increase the hydrophobicity. The interaction between the liquid (water) phase and solid phase (PCL matrix) is energetically unfavourable and the increase in surface roughness, thus, surface area subsequently has a negative effect on wetting [89–91]. Furthermore, SMPs produced through physical milling maintain relatively high contents of the crystalline regions of fibroin with β-sheet hydrophobic domains populating the structure, which results in the hydrophobic nature of the SMPs [92,93]. The

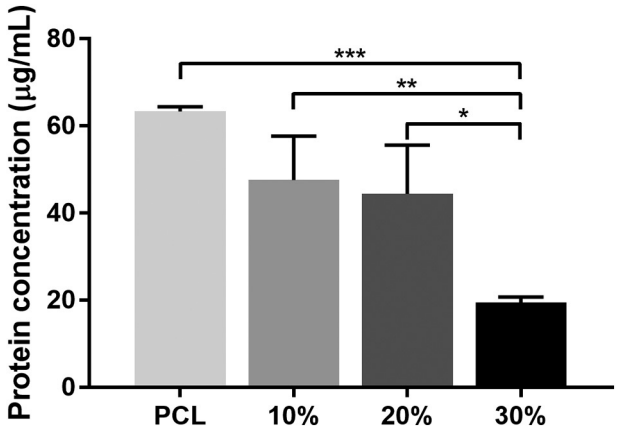

Fig. 8. Protein adsorption of the PCL/SMP scaffolds after incubation in a 10% FBS solution for 12 h.

incorporation of SMPs have been shown to increase the hydrophilicity of a chitosan hydrogel [33]. However, as chitosan is hydrophilic the increase in surface roughness by inclusion of SMPs promotes energetically favourable interactions thus an increase in wettability.

3.7. Protein adsorption

The total amount of protein adsorbed onto the composite surface was determined through immersion of the scaffolds in a 10% FBS solution for 12 h (Fig. 8). Control samples incubated in PBS show a large amount of protein (fibroin) present on the SMP containing samples with the protein quantity following the trend of increasing SMP loading and no protein observed on PCL only scaffolds (Fig. S5 – supplementary information). This allows a method to quantify the amount of fibroin protein at the surface; the experimental samples were normalised to these controls. The results show a decreasing trend in protein adsorption with higher SMP loading in the scaffolds. The 30 wt% SMP scaffolds have significantly lower protein adsorption than all other scaffold types whilst 10 wt% and 20 wt% SMP scaffolds have similar quantities of protein adsorbed.

Typically, hydrophobic materials can adsorb more protein than hydrophilic surfaces [94,95]. The binding of protein on hydrophilic surfaces requires the displacement of water, which creates an energy barrier which must be overcome. Although hydrophobic surfaces can bind through internal hydrophobic domains in the protein this can lead to unfolding and denaturing of the protein. Subsequently, understanding the protein adsorption kinetics, conformation at the surface, and adhesion strength are important factors in determining cell behaviour. Bovine serum albumin is a major component of FBS and has been shown to have increased adhesion on surfaces with contact angles higher than ~60–65° [96]. The SMP scaffolds reduce the amount of protein adsorbed even though they are more hydrophobic than the PCL only scaffolds. The increase in roughness should also enhance the available surface area for protein binding.

The presence of silk fibroin, predominately as crystalline β-sheets in the SMPs, may minimise protein adsorption onto the PCL surface. Protein adsorption onto differently processed silk cast films showed that higher crystallinity and hydrophobicity reduced protein adsorption [97]. Thus, the highly crystalline and hydrophobic SMPs may reduce protein affinity for the surface and decrease the available surface area for protein adsorption. The kinetics and specific protein adsorption need to be evaluated to understand the mechanism of protein binding on SMPs and the composite material scaffold, thus, subsequently how protein adsorption influences material-cell interactions.

3.8. Enzymatic degradation

The main degradation route for PCL is hydrolysis of ester bonds which is highly reliant on material crystallinity and water uptake thus in typical *in vitro* and *in vivo* conditions is slow [9,14,98]. Accelerated degradation model studies using chemical or enzymatic methods are necessary to ascertain the role that material fillers such as SMPs have on the degradation profile of a PCL-based composite and can also be used to determine any cytotoxicity associated with degradation by-products [9,55,99–101]. The PCL/SMP scaffolds degradation profiles were evaluated using a model accelerated enzymatic method employing a lipase from *Thermomyces lanuginosus*. The change in scaffold mass, morphology, and surface corrosion are investigated (Figs. 9 and 10).

Control groups immersed in PBS buffer showed no apparent change in mass which indicates that hydrolytic degradation of the scaffolds did not occur. This is expected as PCL shows little hydrolytic degradation in PBS or water for up to a year [14,15]. In the enzymatic degradation solution, pure PCL scaffolds showed the highest stability throughout the whole period. The presence of SMPs in the composite scaffolds accelerated the degradation process; all PCL/SMP scaffolds lost their scaffolding structure within 3 days. By day 3 all PCL/SMP scaffolds were fully collapsed and the sample degradation solution appeared turbid due to the release of the SMPs, whilst 20% of the original PCL weight remained (Fig. 9b and c). The degradation rate observed for PCL/SMP scaffolds with different silk loadings were not statistically significant.

Structural changes in scaffold morphology were observed during the degradation process (Fig. 9a). All scaffolds changed in appearance within 6 h of enzymatic degradation, with a less shiny appearance possibly reflecting the loss of PCL at the surface and the appearance of more SMPs (observed as white particles) exposed on the scaffold surfaces. After 48 h degradation, the scaffolds exhibited uneven fibre edges due to enzyme corrosion. All scaffold fibres appeared thinner compared to the original structures. The PCL/SMP scaffolds had the greatest fibre diameter reduction (with only 1/2 or 1/3 remaining) compared to pure PCL scaffolds. Correspondingly, inter-fibre pores became larger and delamination between adjacent layers occurring with some fibres becoming detached from the scaffolds.

To observe the degradation process in more detail, single fibre surface morphology and height changes were recorded for each scaffold (Fig. 10). The fibre surface progressively became rougher and the fibre diameter decreased. The enzymatic degradation of the scaffolds creates holes in the scaffold surface; as lipase only degrades PCL when the holes in the PCL matrix became larger than the size of the embedded SMPs, these particles become detached and released into solution. Thus, as the SMPs are released this increases the available surface area within the PCL matrix for the enzyme to degrade which increases the degradation rate. As the printed fibres were optimised for the same diameter, the high SMP loading scaffolds contained less PCL, which will then also lead to increased scaffold degradability.

Furthermore, the reduced crystallinity of PCL after SMP inclusion, as previously described, could make the PCL more prone to degradation by lipase. Several studies on the degradation behaviour of PCL suggest that the degradation process is selective, with the amorphous regions being attacked and degraded prior to the crystalline regions. The proposed explanation is the sufficient spatial degree of freedom in the amorphous regions that allows better penetration of the enzyme into the polymer chains [102,103].

Polymer scaffold degradation is a chemical/biological cleavage process of polymer chains into oligomers, monomers or other low molecular weight degradation product that will eventually be metabolised and removed [14,104].The degradation rate of pure PCL is slow (up to several years *in vivo*) compared to other biopolymers, which can cause issues depending on the specific tissue engineering application requirements [12,105,106]. As a key goal is matching the degradation rate with the rate of new tissue formation, the faster rates of

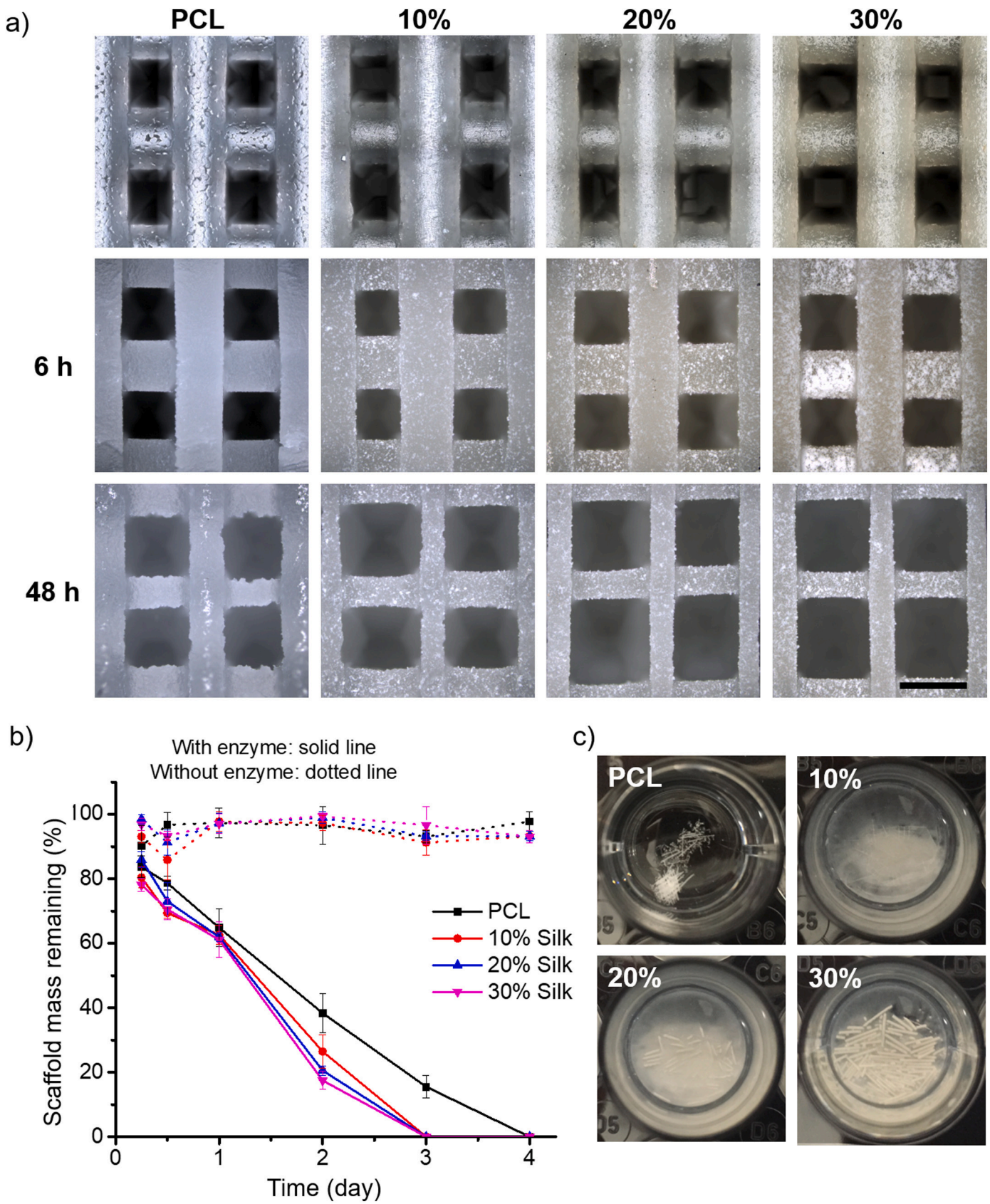

Fig. 9. Accelerated enzymatic degradation of the PCL/SMP scaffolds. a) Microscopy images of the scaffolds before and after 6 and 48 h degradation with SMPs appearing as white particles in the degraded scaffolds (scale = 400 μm). b) Degradation profile of scaffold mass remaining up to 4 days with and without enzyme. c) Images of the scaffolds in the enzyme solution at day 3.

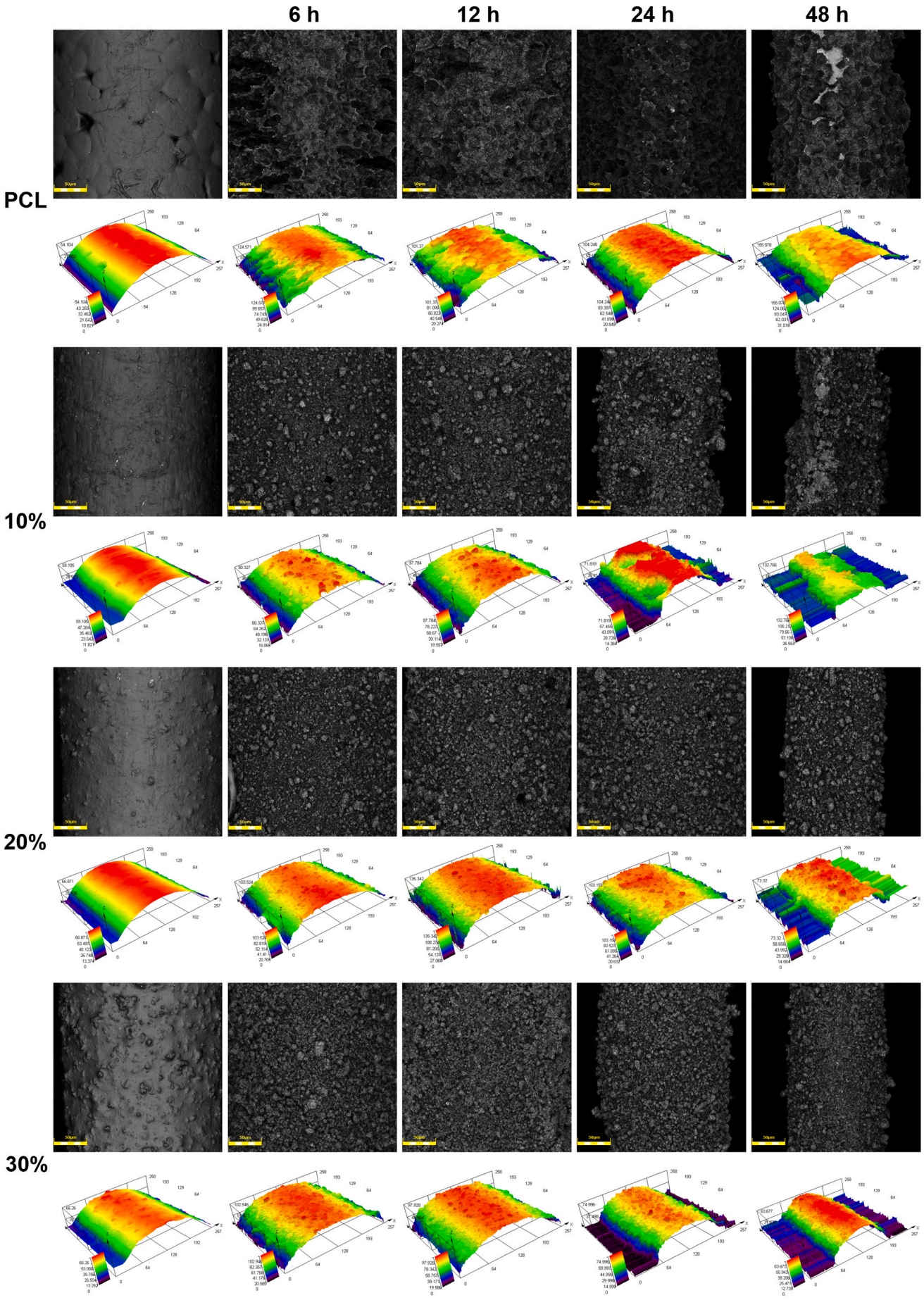

(caption on next page)

Fig. 10. Surface degradation topography and height profile (scale bar = 50 μm; height mapping scan size = 257 × 258 μm).

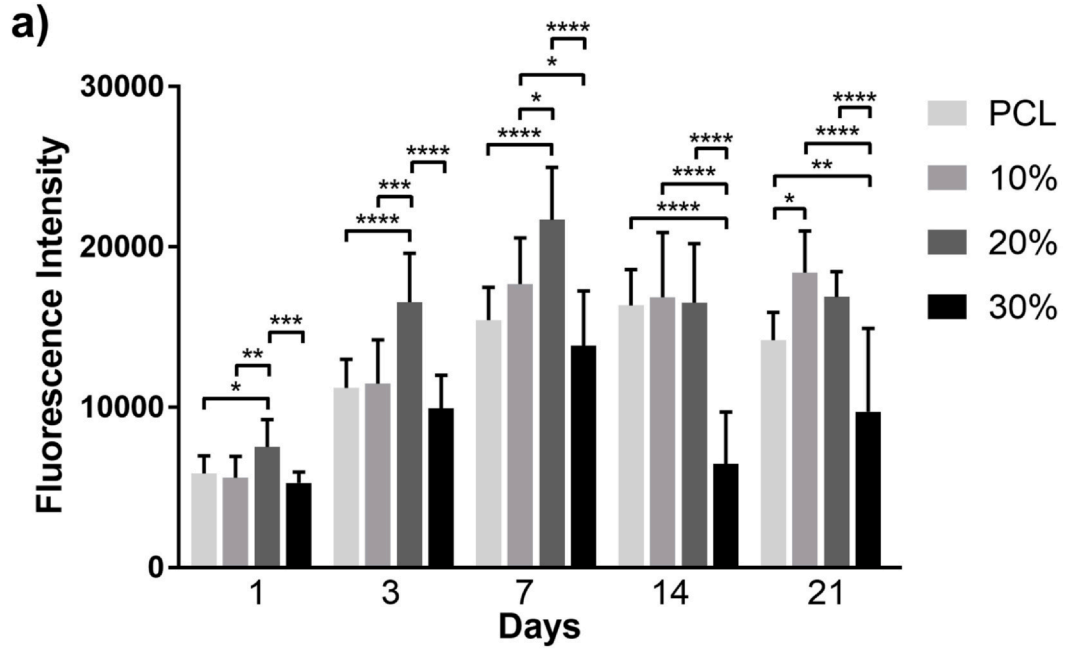

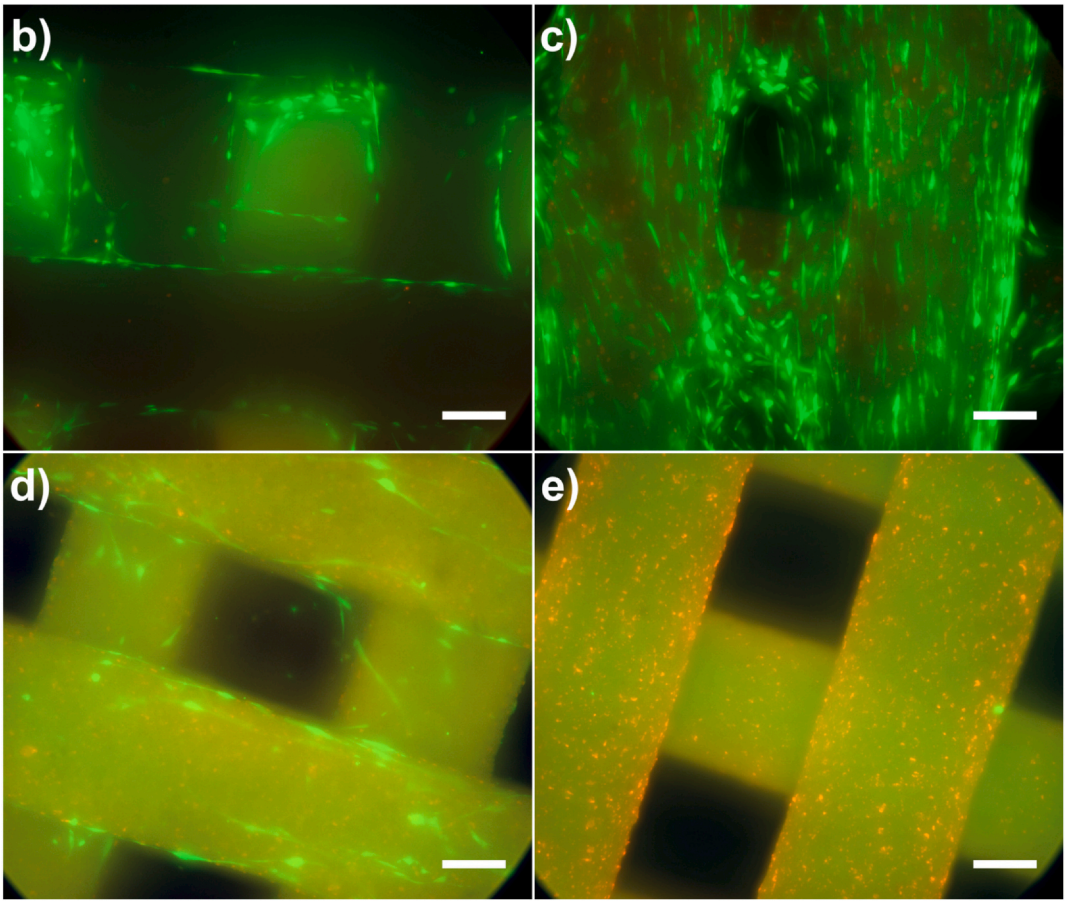

Fig. 11. a) Cell metabolic activity on the PCL/SMP scaffolds at day 1, 3, 7, 14, and 21. Cell viability on b) PCL, c) 10 wt%, d) 20 wt%, and e) 30 wt% SMP scaffolds at day 21 (scale = 100 μm).

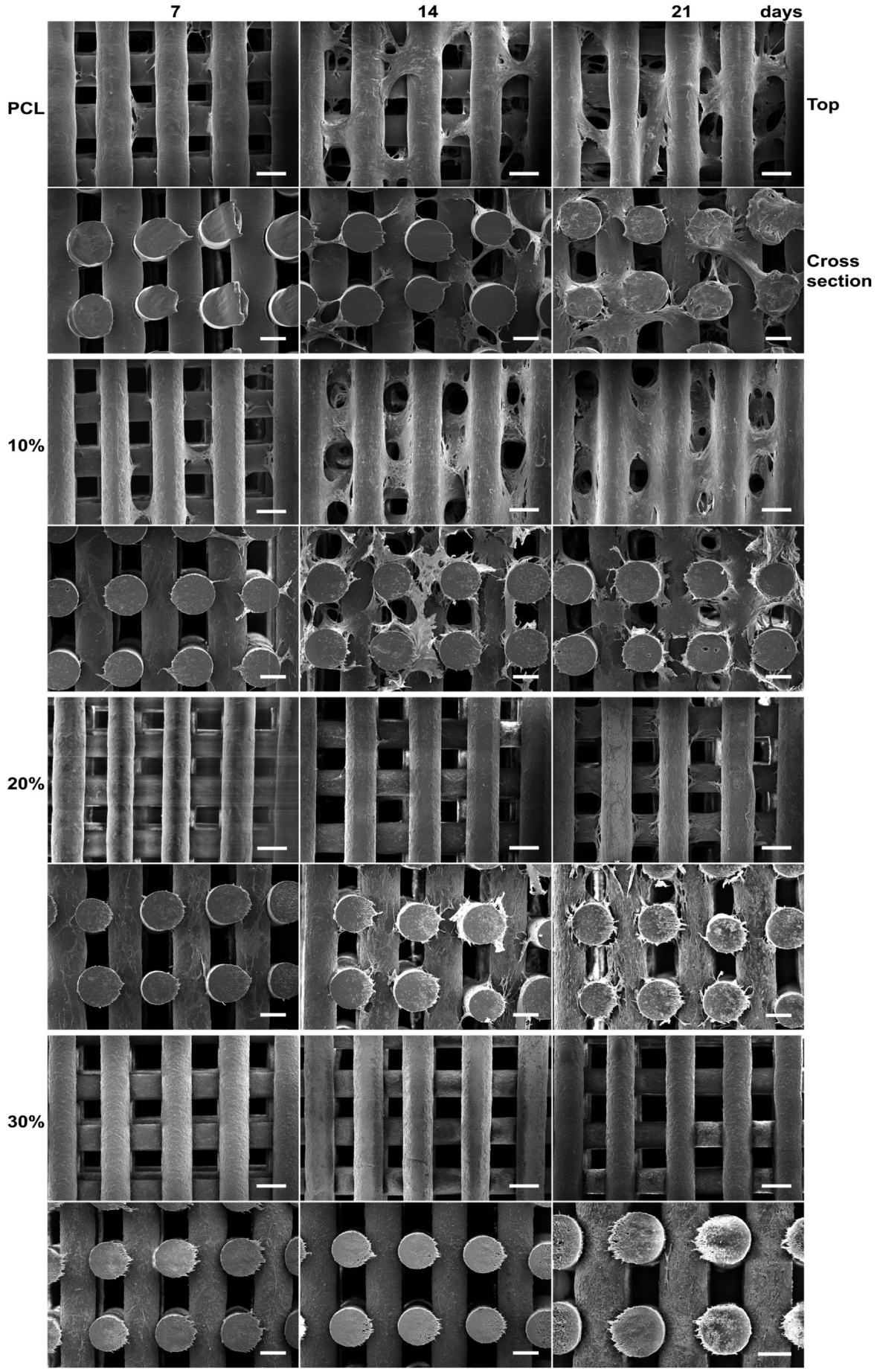

(caption on next page)

Fig. 12. Cell morphology of the hADSC seeded PCL/SMP scaffolds at day 7, 14, and 21 with top-view (scale = 300 μm) and cross-section (scale = 200 μm) as observed by SEM.

degradation brought by the addition of SMPs could be advantageous compared to pure PCL scaffolds. Nonetheless, how these results will translate to *in vivo* behaviour is unclear and further animal testing is required to evaluate if the introduction of SMPs can translate to improved degradation rates and to understand if there any adverse effects from the released SMPs.

3.9. Biological assessment

The PCL/SMP scaffolds have been initially biologically assessed by the seeding and culture of hADSCs for up to 21 days *in vitro* and the cell metabolic activity, viability, and morphology was evaluated (Figs. 11 and 12).

Cell metabolic activity increased in all scaffolds, as measured by an increase in the fluorescence intensity through the Alamar Blue assay, up till day 7 (Fig. 11a). At day 7, the 20 wt% SMP scaffolds had the highest fluorescence intensity whilst the 30 wt% had the lowest. A slight decrease and stabilisation in fluorescence intensity is observed by day 14 and 21 in the PCL, 10 wt%, and 20 wt% SMP scaffolds which can be attributed to a confluent state being reached and a reduction of the metabolic activity of the cells. The 10 wt% SMP scaffolds had the highest fluorescence intensity by day 21. However, a significant reduction in fluorescence intensity is observed for the 30 wt% SMP scaffolds between day 7 and 14 which then remains stable till day 21. This decrease can potentially be attributed to material cytotoxicity at high concentrations of SMPs and reduction in cell numbers.

Cell viability was observed at day 21 using a live/dead assay, which indicates that the PCL, 10 wt%, and 20 wt% SMP scaffolds support viable cells (Fig. 11b–d). The observation of dead cells was complicated due to the SMPs binding EthD-1 stain, as previously described (Fig. S2), thus the determination of the number of unviable cells was not possible. The 30 wt% SMP scaffolds showed only a few observable viable cells in the entire scaffold (Fig. 11e).

Cell morphology, spreading and migration throughout the scaffolds was observed using SEM at day 7, 14, and 21 (Fig. 12). The PCL, 10 wt %, and 20 wt% SMP scaffolds all supported considerable cell proliferation and migration throughout the scaffolds by day 21, as demonstrated by the presence of cells throughout the scaffold cross-section and not concentrated in a specific location. Only a few cells are observable at all-time points for the 30 wt% SMP scaffolds. The PCL and 10 wt% SMP scaffolds show dense cell and ECM formation by day 14 and at day 21, especially in the 10 wt% SMP scaffolds, the pores are beginning to become blocked due to cell proliferation and ECM deposition. Most noticeably is the different cell morphology observed on the 20 wt% SMP scaffolds. The hADSCs are tightly bound to the fibre surface forming dense sheets across the fibres surface whilst the cells in the PCL and 10 wt% SMP scaffolds show considerably more spreading, bridging between fibres, and ECM production. A similar tightly bound cell morphology is observed on the 30 wt% SMP scaffolds at day 21. The difference in cell morphology, spreading, and migration observed on the scaffolds may be due to changes in the surface properties of the scaffold as a result of SMPs increasing the surface stiffness and roughness, hydrophobicity, and reducing the amount of protein adsorbed. This will change the cell-material interactions *via* the adsorbed proteins and subsequently the presentation of integrin binding clusters which will influence cell behaviour [107]. The distribution of the SMPs at the PCL matrix surface will alter the distribution and conformation of the adsorbed proteins, furthermore, the stiffer surface of the SMP will alter mechanotransduction pathways within the cells, which may be conducive for promoting osteogenic differentiation [77–79].

A significant feature observed was the formation of small particles (< 1 μm) and a crust-like layer on the 20 wt% and 30 wt% SMP scaffolds by at least day 14 (Figs. 12 and 13). EDX analysis of the particles shows the presence of calcium which is not observed in the surrounding area where no particles or crust are present. Silk fibroin has been demonstrated to regulate the nucleation and mineralisation of calcium phosphates such as hydroxyapatite [41–43,108–114]. The presence of SMPs may act as a nucleating point and allow precipitation and calcium mineralisation from the cell culture medium. The amorphous regions of silk between the crystalline β-sheets have been shown to be responsible for nucleating hydroxyapatite in a similar process to collagen type I in bone [112]. Although the SMPs are highly rich in crystalline β-sheets, amorphous regions are still present. Additionally, the change in cell morphology observed between 10 wt% and 20 wt% SMP scaffolds could be related to the hADSCs undergoing osteogenic differentiation due to the high presence of a calcium-based mineral. Furthermore, silk fibroin is composed primarily of glycine and alanine and these are the principal degradation by-products which can be utilised for neo-protein synthesis, potentially supporting the increase in cell proliferation observed in this study [25].

Further investigation is required to elucidate the mechanism of calcium mineral formation, the specific form of calcium, and if the process is spontaneous or cell mediated. At higher SMP loading the mineralisation process becomes more obvious. Furthermore, the adverse cellular response observed at high SMP loading may be related to the calcium mineralisation, which may cause physical damage to the cells or due to an increase in the intracellular or local intercellular calcium ion concentration, further study is required to understand this phenomenon. Additionally, the degradation of the SMPs into smaller fragments, silk nanoparticles, during the cell culture period may induce a cytotoxic effect at high concentrations as Naserzadeh et al. have demonstrated during cell culture of fibroblasts and human umbilical vein endothelial cells incubated with silk nanoparticles [115]. This observation is also in agreement with a previous study on cytotoxicity of silk nanoparticles that at low concentrations showed no cytotoxicity, whereas a decrease in cell viability was observed with higher concentrations [116]. Thus, further investigation is required to determine the optimum silk loading in the composites and the influence of SMP degradation has on biocompatibility. Furthermore, the influence of SMPs and calcium nucleation requires *in vivo* investigation to determine how the material responds in a complex biological environment and subsequent cell and tissue response.

The results indicate that the PCL, 10 wt%, and 20 wt% SMP scaffolds support metabolically active and viable cells which can proliferate up to day 21 whilst the 30 wt% SMP scaffold exhibits a cytotoxic behaviour from at least day 7. The 10 wt% and 20 wt% SMP scaffolds show equal or better biocompatibility than PCL alone. Although a cytotoxic behaviour is observed at the highest particle loading, the scaffolds at 10 wt% exhibited significant advantages in terms of mechanical reinforcement, increased degradation rate, and cell proliferation thus higher SMP loadings may not be necessary to achieve the desired impact. The 3D printed PCL/SMP scaffolds show potential suitability for load bearing applications such as bone or cartilage tissue engineering. However, further understanding of the influence of SMPs on the osteogenic or chondrogenic differentiation of hADSCs is required.

4. Conclusion

This study demonstrates the development and characterisation of a new composite material, a PCL blended with SMPs. The composite material has been used to fabricate scaffolds for bone tissue engineering applications using screw-assisted extrusion-based 3D printing. The rheological behaviour of the PCL/SMP composite showed an increase in material elasticity and shear-thinning behaviour. Scaffolds were

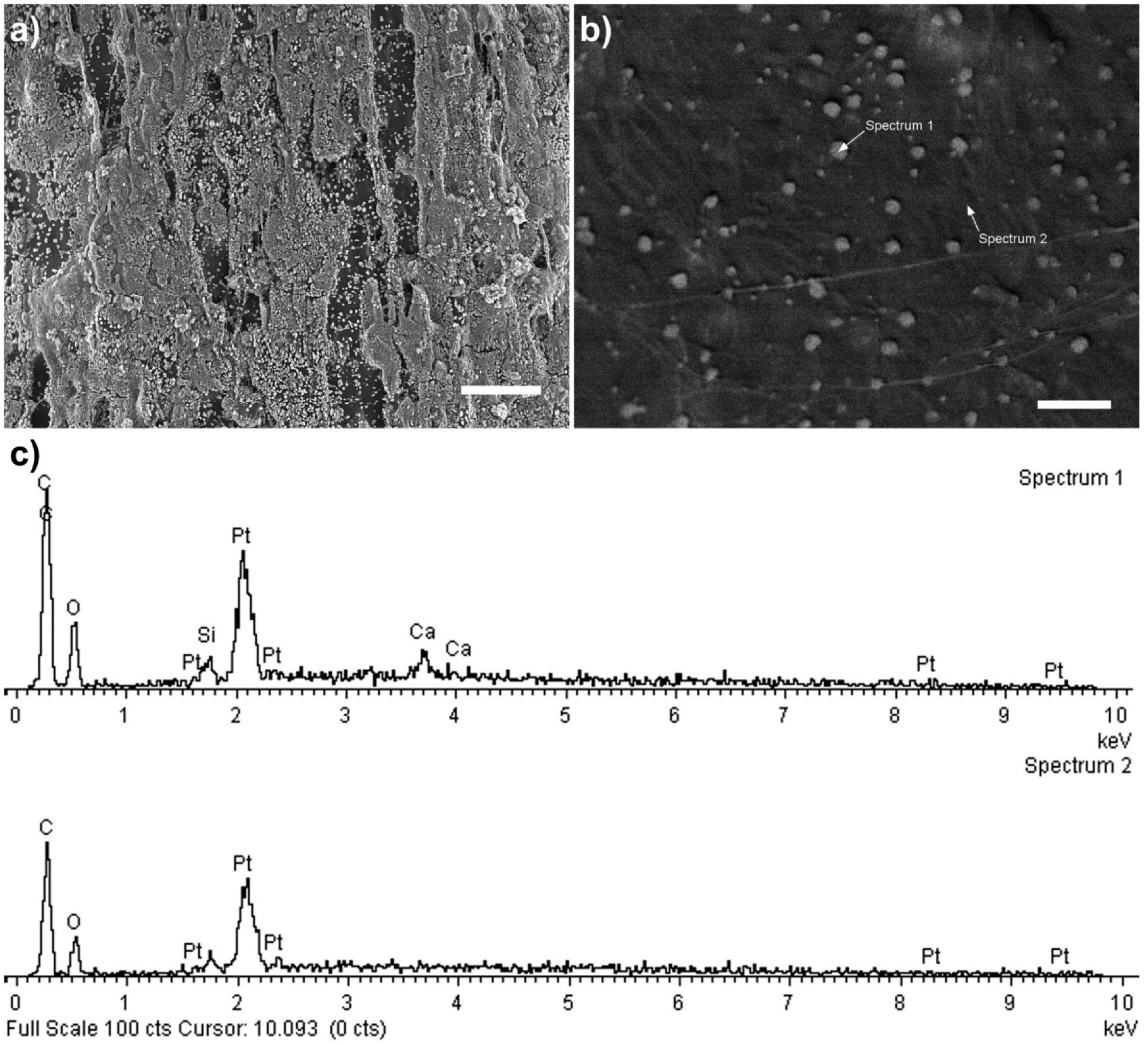

Fig. 13. EDX analysis of the PCL/SMP scaffolds after cell culture of 14 days. a) Representative SEM image of 30 wt% SMP scaffold showing surface particle deposition forming a crust layer (scale = 20 μm). b) Backscattered electron image of deposited particles and location of spectrum 1 and 2 (scale = 5 μm). EDX spectrum 1 (particle) and spectrum 2 (scaffold surface).

successfully fabricated up to 30 wt% SMP loading and showed uniform morphology. The incorporation of SMPs reinforced the PCL matrix improving the mechanical properties of the scaffolds and are within the lower region of trabecular bone mechanical properties. The scaffold showed increasing roughness and hydrophobicity with higher SMP loading due to the highly crystalline β-sheets in the SMPs. The presence of SMPs accelerated the enzymatic degradation of the scaffolds. A clear difference is observed in material properties with all SMP containing samples compared to PCL alone typically correlating to increasing SMP content. However, the mechanical and protein adsorption properties follow a non-proportional trend for 10 wt% and 20 wt% which have similar values, further investigation is required to understand this behaviour. Preliminary biocompatibility studies showed that hADSCs were viable and proliferated up to 21 days on scaffolds up to 20 wt% SMP loading, however, 30 wt% SMP scaffolds exhibited cytotoxicity. Considerable calcium mineral deposition was observed on the SMP scaffolds as silk facilitates the nucleation and mineralisation of calcium, further investigation is required to determine how this influences the osteogenic differentiation of hADSCs. The presence of SMPs in the scaffolds significantly improved the degradation rate, mechanical properties, and cell proliferation of the scaffolds indicating that key disadvantages of PCL can be improved by incorporating silk particles.

The results demonstrate that the 3D printed PCL scaffolds reinforced with SMPs have improved degradation and mechanics with potential osteogenic properties. This study offers a promising alternative approach to overcome limitations associated with PCL-based scaffolds for load bearing tissue regeneration.

CRediT authorship contribution statement

Cian Vyas: Investigation, Methodology, Formal analysis, Visualization, Writing - original draft, Writing - review & editing, Conceptualization. **Jun Zhang:** Investigation, Methodology, Formal analysis, Visualization, Writing - review & editing, Conceptualization. **Øystein Øvrebø:** Investigation, Formal analysis, Writing - review & editing. **Boyang Huang:** Investigation, Formal analysis, Writing - review & editing. **Iwan Roberts:** Investigation, Formal analysis, Writing - review & editing. **Mohan Setty:** Investigation, Formal analysis, Writing - review & editing. **Benjamin Allardyce:** Supervision, Methodology, Writing - review & editing, Conceptualization, Validation. **Håvard Haugen:** Investigation, Formal analysis, Visualization, Writing - review & editing, Validation. **Rangam Rajkhowa:** Supervision, Methodology, Writing - review & editing, Conceptualization, Funding acquisition, Validation. **Paulo Bartolo:** Supervision, Methodology, Writing - review & editing, Conceptualization, Funding acquisition, Project administration, Validation.

Declaration of competing interest

The authors declare that they have no known competing financial interests or personal relationships that could have appeared to influence the work reported in this paper.

Acknowledgements

The authors wish to acknowledge the funding provided by the Engineering and Physical Sciences Research Council (EPSRC) and Medical Research Council (MRC) Centre for Doctoral Training in Regenerative Medicine (EP/L014904/1). The authors would also like to thank Mr. Andrew Wallwork, University of Manchester, for his expertise in particle characterisation.

Appendix A. Supplementary data

Supplementary data to this article can be found online at https://doi.org/10.1016/j.msec.2020.111433.

References

[1] F.P.W. Melchels, M.A.N. Domingos, T.J. Klein, J. Malda, P.J. Bartolo, D.W. Hutmacher, Additive manufacturing of tissues and organs, Prog. Polym. Sci. 37 (8) (2012) 1079–1104.
[2] S. Derakhshanfar, R. Mbeleck, K. Xu, X. Zhang, W. Zhong, M. Xing, 3D bioprinting for biomedical devices and tissue engineering: a review of recent trends and advances, Bioactive Materials. 3 (2) (2018) 144–156.
[3] H. Ma, C. Feng, J. Chang, C. Wu, 3D-printed bioceramic scaffolds: from bone tissue engineering to tumor therapy, Acta Biomater. 79 (2018) 37–59.
[4] C. Vyas, G. Poologasundarampillai, J. Hoyland, P. Bartolo, 3D printing of biocomposites for osteochondral tissue engineering, Ambrosio L, editor, Woodhead Publishing, Biomedical Composites (Second Edition), 2017, pp. 261–302.
[5] B. Duan, State-of-the-art review of 3D bioprinting for cardiovascular tissue engineering, Ann. Biomed. Eng. 45 (1) (2017) 195–209.
[6] R.F. Pereira, A. Sousa, C.C. Barrias, A. Bayat, P.L. Granja, P.J. Bártolo, Advances in bioprinted cell-laden hydrogels for skin tissue engineering, Biomanufacturing Reviews. 2 (1) (2017) 1.
[7] C. Vyas, R. Pereira, B. Huang, F. Liu, W. Wang, P. Bartolo, Engineering the vasculature with additive manufacturing, Current Opinion in Biomedical Engineering. 2 (2017) 1–13.
[8] X. Ma, J. Liu, W. Zhu, M. Tang, N. Lawrence, C. Yu, et al., 3D bioprinting of functional tissue models for personalized drug screening and in vitro disease modeling, Adv. Drug Deliv. Rev. 132 (2018) 235–251.
[9] M.A. Woodruff, D.W. Hutmacher, The return of a forgotten polymer—polycaprolactone in the 21st century, Prog. Polym. Sci. 35 (10) (2010) 1217–1256.
[10] D. Mondal, M. Griffith, S.S. Venkatraman, Polycaprolactone-based biomaterials for tissue engineering and drug delivery: current scenario and challenges, Int. J. Polym. Mater. Polym. Biomater. 65 (5) (2016) 255–265.
[11] N. Siddiqui, S. Asawa, B. Birru, R. Baadhe, S. Rao, PCL-based composite scaffold matrices for tissue engineering applications, Mol. Biotechnol. 60 (7) (2018) 506–532.
[12] H. Sun, L. Mei, C. Song, X. Cui, P. Wang, The in vivo degradation, absorption and excretion of PCL-based implant, Biomaterials. 27 (9) (2006) 1735–1740.
[13] J.C. Middleton, A.J. Tipton, Synthetic biodegradable polymers as orthopedic devices, Biomaterials. 21 (23) (2000) 2335–2346.
[14] C.X.F. Lam, D.W. Hutmacher, J.-T. Schantz, M.A. Woodruff, S.H. Teoh, Evaluation of polycaprolactone scaffold degradation for 6 months in vitro and in vivo, J. Biomed. Mater. Res. A 90A (3) (2009) 906–919.
[15] D. Lovera, L. Márquez, V. Balsamo, A. Taddei, C. Castelli, A.J. Müller, Crystallization, morphology, and enzymatic degradation of polyhydroxybutyrate/polycaprolactone (PHB/PCL) blends, Macromol. Chem. Phys. 208 (9) (2007) 924–937.
[16] Huang B, Caetano G, Vyas C, Blaker JJ, Diver C, Bártolo P. Polymer-Ceramic Composite Scaffolds: The Effect of Hydroxyapatite and β-tri-Calcium Phosphate. Materials. 2018;11(1).
[17] B. Huang, C. Vyas, I. Roberts, Q.-A. Poutrel, W.-H. Chiang, J.J. Blaker, et al., Fabrication and characterisation of 3D printed MWCNT composite porous scaffolds for bone regeneration, Mater. Sci. Eng. C 98 (2019) 266–278.
[18] W. Wang, G.F. Caetano, W.-H. Chiang, A.L. Braz, J.J. Blaker, M.A.C. Frade, et al., Morphological, mechanical and biological assessment of PCL/pristine graphene scaffolds for bone regeneration, International Journal of Bioprinting. 2 (2) (2016) 204–213.
[19] M.M. Stevens, J.H. George, Exploring and engineering the cell surface interface, Science. 310 (5751) (2005) 1135.
[20] Y.-C. Jiang, L. Jiang, A. Huang, X.-F. Wang, Q. Li, L.-S. Turng, Electrospun polycaprolactone/gelatin composites with enhanced cell–matrix interactions as blood vessel endothelial layer scaffolds, Mater. Sci. Eng. C 71 (2017) 901–908.
[21] Q. Zhang, S. Lv, J. Lu, S. Jiang, L. Lin, Characterization of polycaprolactone/collagen fibrous scaffolds by electrospinning and their bioactivity, Int. J. Biol. Macromol. 76 (2015) 94–101.
[22] P.S.P. Poh, D.W. Hutmacher, B.M. Holzapfel, A.K. Solanki, M.M. Stevens, M.A. Woodruff, In vitro and in vivo bone formation potential of surface calcium phosphate-coated polycaprolactone and polycaprolactone/bioactive glass composite scaffolds, Acta Biomater. 30 (2016) 319–333.
[23] Pertici G, Rossi F, Casalini T, Perale G. Composite polymer-coated mineral grafts for bone regeneration: material characterisation and model study. Annals of Oral & Maxillofacial Surgery. 2014;2(1).
[24] D. D'Alessandro, G. Perale, M. Milazzo, S. Moscato, C. Stefanini, G. Pertici, et al., Bovine bone matrix/poly(l-lactic-co-ε-caprolactone)/gelatin hybrid scaffold (SmartBone®) for maxillary sinus augmentation: a histologic study on bone regeneration, Int. J. Pharm. 523 (2) (2017) 534–544.
[25] P. Bhattacharjee, B. Kundu, D. Naskar, H.-W. Kim, T.K. Maiti, D. Bhattacharya, et al., Silk scaffolds in bone tissue engineering: an overview, Acta Biomater. 63 (2017) 1–17.
[26] L.-D. Koh, Y. Cheng, C.-P. Teng, Y.-W. Khin, X.-J. Loh, S.-Y. Tee, et al., Structures, mechanical properties and applications of silk fibroin materials, Prog. Polym. Sci. 46 (2015) 86–110.
[27] S. Chawla, S. Midha, A. Sharma, S. Ghosh, Silk-based bioinks for 3D bioprinting, Advanced Healthcare Materials. 7 (8) (2018) 1701204.
[28] J. Melke, S. Midha, S. Ghosh, K. Ito, S. Hofmann, Silk fibroin as biomaterial for bone tissue engineering, Acta Biomater. 31 (2016) 1–16.
[29] Mu X, Wang Y, Guo C, Li Y, Ling S, Huang W, et al. 3D printing of silk protein structures by aqueous solvent-directed molecular assembly. Macromol. Biosci. 2019;0(0):1900191.
[30] Z. Zheng, J. Wu, M. Liu, H. Wang, C. Li, M.J. Rodriguez, et al., 3D bioprinting of self-standing silk-based bioink, Advanced Healthcare Materials. 7 (6) (2018) 1701026.
[31] S. Chawla, A. Kumar, P. Admane, A. Bandyopadhyay, S. Ghosh, Elucidating role of silk-gelatin bioink to recapitulate articular cartilage differentiation in 3D bioprinted constructs, Bioprinting. 7 (2017) 1–13.
[32] J. Zhang, B.J. Allardyce, R. Rajkhowa, Y. Zhao, R.J. Dilley, S.L. Redmond, et al., 3D printing of silk particle-reinforced chitosan hydrogel structures and their properties, ACS Biomaterials Science & Engineering. 4 (8) (2018) 3036–3046.
[33] J. Zhang, B.J. Allardyce, R. Rajkhowa, S. Kalita, R.J. Dilley, X. Wang, et al., Silk particles, microfibres and nanofibres: a comparative study of their functions in 3D printing hydrogel scaffolds, Mater. Sci. Eng. C 103 (2019) 109784.
[34] N. Bhardwaj, R. Rajkhowa, X. Wang, D. Devi, Milled non-mulberry silk fibroin microparticles as biomaterial for biomedical applications, Int. J. Biol. Macromol. 81 (2015) 31–40.
[35] D.N. Rockwood, E.S. Gil, S.-H. Park, J.A. Kluge, W. Grayson, S. Bhumiratana, et al., Ingrowth of human mesenchymal stem cells into porous silk particle reinforced silk composite scaffolds: an in vitro study, Acta Biomater. 7 (1) (2011) 144–151.
[36] B.B. Mandal, A. Grinberg, E. Seok Gil, B. Panilaitis, D.L. Kaplan, High-strength silk protein scaffolds for bone repair, Proc. Natl. Acad. Sci. 109 (20) (2012) 7699.
[37] P. Gupta, M. Adhikary, M. JC, M. Kumar, N. Bhardwaj, B.B. Mandal, Biomimetic, osteoconductive non-mulberry silk fiber reinforced tricomposite scaffolds for bone tissue engineering, ACS Appl. Mater. Interfaces 8 (45) (2016) 30797–30810.
[38] S.-Y. Fu, X.-Q. Feng, B. Lauke, Y.-W. Mai, Effects of particle size, particle/matrix interface adhesion and particle loading on mechanical properties of particulate–polymer composites, Compos. Part B 39 (6) (2008) 933–961.
[39] S. Ahmed, F.R. Jones, A review of particulate reinforcement theories for polymer composites, J. Mater. Sci. 25 (12) (1990) 4933–4942.
[40] R. Rajkhowa, E.S. Gil, J. Kluge, K. Numata, L. Wang, X. Wang, et al., Reinforcing silk scaffolds with silk particles, Macromol. Biosci. 10 (6) (2010) 599–611.
[41] Y. Jin, B. Kundu, Y. Cai, S.C. Kundu, J. Yao, Bio-inspired mineralization of hydroxyapatite in 3D silk fibroin hydrogel for bone tissue engineering, Colloids Surf. B: Biointerfaces 134 (2015) 339–345.
[42] R. Kino, T. Ikoma, A. Monkawa, S. Yunoki, M. Munekata, J. Tanaka, et al., Deposition of bone-like apatite on modified silk fibroin films from simulated body fluid, J. Appl. Polym. Sci. 99 (5) (2006) 2822–2830.
[43] J.R. Vetsch, S.J. Paulsen, R. Müller, S. Hofmann, Effect of fetal bovine serum on mineralization in silk fibroin scaffolds, Acta Biomater. 13 (2015) 277–285.
[44] Weska RF, Nogueira GM, Vieira WC, Beppu MM. Porous Silk Fibroin Membrane as a Potential Scaffold for Bone Regeneration. Key Engineering Materials. 2009;396–398:187–90.
[45] L. Meinel, V. Karageorgiou, R. Fajardo, B. Snyder, V. Shinde-Patil, L. Zichner, et al., Bone tissue engineering using human mesenchymal stem cells: effects of scaffold material and medium flow, Ann. Biomed. Eng. 32 (1) (2004) 112–122.
[46] L. Meinel, R. Fajardo, S. Hofmann, R. Langer, J. Chen, B. Snyder, et al., Silk implants for the healing of critical size bone defects, Bone. 37 (5) (2005) 688–698.
[47] Liu F, Mishbak H, Bartolo Pjd. Hybrid polycaprolactone/hydrogel scaffold fabrication and in-process plasma treatment using PABS. International Journal of Bioprinting; Vol 5, No 1 (2019). 2019.
[48] B. Huang, C. Vyas, J.J. Byun, M. El-Newehy, Z. Huang, P. Bártolo, Aligned multiwalled carbon nanotubes with nanohydroxyapatite in a 3D printed polycaprolactone scaffold stimulates osteogenic differentiation, Mater. Sci. Eng. C 108 (2020) 110374.
[49] Z. Meng, J. He, Z. Cai, M. Zhang, J. Zhang, R. Ling, et al., In-situ re-melting and re-solidification treatment of selective laser sintered polycaprolactone lattice scaffolds for improved filament quality and mechanical properties, Biofabrication. 12 (3) (2020) 035012.
[50] A. Mazzoli, C. Ferretti, A. Gigante, E. Salvolini, M. Mattioli-Belmonte, Selective

laser sintering manufacturing of polycaprolactone bone scaffolds for applications in bone tissue engineering, Rapid Prototyp. J. 21 (4) (2015) 386–392.
[51] B.J. Allardyce, R. Rajkhowa, R.J. Dilley, S.L. Redmond, M.D. Atlas, X. Wang, Glycerol-plasticised silk membranes made using formic acid are ductile, transparent and degradation-resistant, Mater. Sci. Eng. C 80 (2017) 165–173.
[52] R. Rajkhowa, L. Wang, J. Kanwar, X. Wang, Fabrication of ultrafine powder from eri silk through attritor and jet milling, Powder Technol. 191 (1) (2009) 155–163.
[53] Cox W, Merz E, editors. Rheology of polymer melts—A correlation of dynamic and steady flow measurements. International Symposium on Plastics Testing and Standardization; 1959: ASTM International.
[54] J. Kong, Y. Yu, X. Pei, C. Han, Y. Tan, L. Dong, Polycaprolactone nanocomposite reinforced by bioresource starch-based nanoparticles, Int. J. Biol. Macromol. 102 (2017) 1304–1311.
[55] D. Ju, L. Han, F. Li, S. Chen, L. Dong, Crystallization, mechanical properties, and enzymatic degradation of biodegradable poly(ε-caprolactone) composites with poly(lactic acid) fibers, Polym. Compos. 34 (10) (2013) 1745–1752.
[56] H. Tiainen, S.P. Lyngstadaas, J.E. Ellingsen, H.J. Haugen, Ultra-porous titanium oxide scaffold with high compressive strength, J. Mater. Sci. Mater. Med. 21 (10) (2010) 2783–2792.
[57] H.-B. Wu, H.J. Haugen, E. Wintermantel, Supercritical CO2 in injection molding can produce open porous polyurethane scaffolds – a parameter study, J. Cell. Plast. 48 (2) (2012) 141–159.
[58] W.C. Oliver, G.M. Pharr, Measurement of hardness and elastic modulus by instrumented indentation: advances in understanding and refinements to methodology, J. Mater. Res. 19 (1) (2004) 3–20.
[59] W.C. Oliver, G.M. Pharr, An improved technique for determining hardness and elastic modulus using load and displacement sensing indentation experiments, J. Mater. Res. 7 (6) (1992) 1564–1583.
[60] A. Nandakumar, Z. Tahmasebi Birgani, D. Santos, A. Mentink, N. Auffermann, K. van der Werf, et al., Surface modification of electrospun fibre meshes by oxygen plasma for bone regeneration, Biofabrication. 5 (1) (2012) 015006.
[61] J.M. Sobral, S.G. Caridade, R.A. Sousa, J.F. Mano, R.L. Reis, Three-dimensional plotted scaffolds with controlled pore size gradients: effect of scaffold geometry on mechanical performance and cell seeding efficiency, Acta Biomater. 7 (3) (2011) 1009–1018.
[62] R. Krishnamoorti, E.P. Giannelis, Rheology of end-tethered polymer layered silicate Nanocomposites, Macromolecules. 30 (14) (1997) 4097–4102.
[63] B. Lepoittevin, M. Devalckenaere, N. Pantoustier, M. Alexandre, D. Kubies, C. Calberg, et al., Poly(ε-caprolactone)/clay nanocomposites prepared by melt intercalation: mechanical, thermal and rheological properties, Polymer. 43 (14) (2002) 4017–4023.
[64] B. Huang, P.J. Bártolo, Rheological characterization of polymer/ceramic blends for 3D printing of bone scaffolds, Polym. Test. 68 (2018) 365–378.
[65] M.M. Rueda, M.-C. Auscher, R. Fulchiron, T. Périé, G. Martin, P. Sonntag, et al., Rheology and applications of highly filled polymers: a review of current understanding, Prog. Polym. Sci. 66 (2017) 22–53.
[66] D. Kołbuk, P. Sajkiewicz, K. Maniura-Weber, G. Fortunato, Structure and morphology of electrospun polycaprolactone/gelatine nanofibres, Eur. Polym. J. 49 (8) (2013) 2052–2061.
[67] H.R. Pant, M.P. Neupane, B. Pant, G. Panthi, H.-J. Oh, M.H. Lee, et al., Fabrication of highly porous poly (ε-caprolactone) fibers for novel tissue scaffold via water-bath electrospinning, Colloids Surf. B: Biointerfaces 88 (2) (2011) 587–592.
[68] X. Xu, F. Liu, L. Jiang, J.Y. Zhu, D. Haagenson, D.P. Wiesenborn, Cellulose nanocrystals vs. cellulose nanofibrils: a comparative study on their microstructures and effects as polymer reinforcing agents, ACS Appl. Mater. Interfaces 5 (8) (2013) 2999–3009.
[69] M.J. Gupte, W.B. Swanson, J. Hu, X. Jin, H. Ma, Z. Zhang, et al., Pore size directs bone marrow stromal cell fate and tissue regeneration in nanofibrous macroporous scaffolds by mediating vascularization, Acta Biomater. 82 (2018) 1–11.
[70] C.M. Murphy, M.G. Haugh, F.J. O'Brien, The effect of mean pore size on cell attachment, proliferation and migration in collagen–glycosaminoglycan scaffolds for bone tissue engineering, Biomaterials. 31 (3) (2010) 461–466.
[71] C.M. Murphy, F.J. O'Brien, Understanding the effect of mean pore size on cell activity in collagen-glycosaminoglycan scaffolds, Cell Adhes. Migr. 4 (3) (2010) 377–381.
[72] S.I. Somo, B. Akar, E.S. Bayrak, J.C. Larson, A.A. Appel, H. Mehdizadeh, et al., Pore interconnectivity influences growth factor-mediated vascularization in sphere-templated hydrogels, Tissue Engineering Part C: Methods. 21 (8) (2015) 773–785.
[73] F.P.W. Melchels, A.M.C. Barradas, C.A. van Blitterswijk, J. de Boer, J. Feijen, D.W. Grijpma, Effects of the architecture of tissue engineering scaffolds on cell seeding and culturing, Acta Biomater. 6 (11) (2010) 4208–4217.
[74] F.J. O'Brien, Biomaterials & scaffolds for tissue engineering, Mater. Today 14 (3) (2011) 88–95.
[75] Gariboldi MI, Best SM. Effect of Ceramic Scaffold Architectural Parameters on Biological Response. Frontiers in Bioengineering and Biotechnology. 2015;3(151).
[76] R. Rajkhowa, A. Kafi, Q.T. Zhou, A. Kondor, D.A.V. Morton, X. Wang, Relationship between processing, surface energy and bulk properties of ultrafine silk particles, Powder Technol. 270 (2015) 112–120.
[77] K.A. Jansen, P. Atherton, C. Ballestrem, Mechanotransduction at the cell-matrix interface, Semin. Cell Dev. Biol. 71 (2017) 75–83.
[78] E.K. Paluch, C.M. Nelson, N. Biais, B. Fabry, J. Moeller, B.L. Pruitt, et al., Mechanotransduction: use the force(s), BMC Biol. 13 (1) (2015) 47.
[79] A.J. Engler, S. Sen, H.L. Sweeney, D.E. Discher, Matrix elasticity directs stem cell lineage specification, Cell. 126 (4) (2006) 677–689.
[80] L.J. Gibson, Biomechanics of cellular solids, J. Biomech. 38 (3) (2005) 377–399.
[81] Oftadeh R, Perez-Viloria M, Villa-Camacho JC, Vaziri A, Nazarian A. Biomechanics and Mechanobiology of Trabecular Bone: A Review. Journal of Biomechanical Engineering. 2015;137(1).
[82] J. Zhang, G.L. Niebur, T.C. Ovaert, Mechanical property determination of bone through nano- and micro-indentation testing and finite element simulation, J. Biomech. 41 (2) (2008) 267–275.
[83] P.K. Zysset, X. Edward Guo, C. Edward Hoffler, K.E. Moore, S.A. Goldstein, Elastic modulus and hardness of cortical and trabecular bone lamellae measured by nanoindentation in the human femur, J. Biomech. 32 (10) (1999) 1005–1012.
[84] K. Anselme, L. Ploux, A. Ponche, Cell/material interfaces: influence of surface chemistry and surface topography on cell adhesion, J. Adhes. Sci. Technol. 24 (5) (2010) 831–852.
[85] X. Yao, R. Peng, J. Ding, Cell–material interactions revealed via material techniques of surface patterning, Adv. Mater. 25 (37) (2013) 5257–5286.
[86] H.S. Dhowre, S. Rajput, N.A. Russell, M. Zelzer, Responsive cell–material interfaces, Nanomedicine. 10 (5) (2015) 849–871.
[87] T. Iwata, Y. Doi, Morphology and enzymatic degradation of poly(ε-caprolactone) single crystals: does a polymer single crystal consist of micro-crystals? Polym. Int. 51 (10) (2002) 852–858.
[88] F. Liu, C. Vyas, G. Poologasundarampillai, I. Pape, S. Hinduja, W. Mirihanage, et al., Structural evolution of PCL during melt extrusion 3D printing, Macromol. Mater. Eng. 303 (2) (2018) 1700494.
[89] R.N. Wenzel, Resistance of solid surfaces to wetting by water, Industrial & Engineering Chemistry. 28 (8) (1936) 988–994.
[90] Cassie ABD, Baxter S. Wettability of porous surfaces. Trans. Faraday Soc. 1944;40(0):546–51.
[91] D. Quéré, Rough ideas on wetting, Physica A: Statistical Mechanics and its Applications. 313 (1) (2002) 32–46.
[92] M. Kazemimostaghim, R. Rajkhowa, K. Patil, T. Tsuzuki, X. Wang, Structure and characteristics of milled silk particles, Powder Technol. 254 (2014) 488–493.
[93] C. Vepari, D.L. Kaplan, Silk as a biomaterial, Prog. Polym. Sci. 32 (8) (2007) 991–1007.
[94] K. Wang, C. Zhou, Y. Hong, X. Zhang, A review of protein adsorption on bioceramics, Interface Focus. 2 (3) (2012) 259–277.
[95] I. Firkowska-Boden, X. Zhang, K.D. Jandt, Controlling protein adsorption through nanostructured polymeric surfaces, Advanced Healthcare Materials. 7 (1) (2018) 1700995.
[96] L.-C. Xu, C.A. Siedlecki, Effects of surface wettability and contact time on protein adhesion to biomaterial surfaces, Biomaterials. 28 (22) (2007) 3273–3283.
[97] A. Motta, D. Maniglio, C. Migliaresi, H.-J. Kim, X. Wan, X. Hu, et al., Silk fibroin processing and thrombogenic responses, J. Biomater. Sci. Polym. Ed. 20 (13) (2009) 1875–1897.
[98] L.A. Bosworth, S. Downes, Physicochemical characterisation of degrading polycaprolactone scaffolds, Polym. Degrad. Stab. 95 (12) (2010) 2269–2276.
[99] E. Murray, B.C. Thompson, S. Sayyar, G.G. Wallace, Enzymatic degradation of graphene/polycaprolactone materials for tissue engineering, Polym. Degrad. Stab. 111 (2015) 71–77.
[100] D.N. Bikiaris, Nanocomposites of aliphatic polyesters: an overview of the effect of different nanofillers on enzymatic hydrolysis and biodegradation of polyesters, Polym. Degrad. Stab. 98 (9) (2013) 1908–1928.
[101] C.X.F. Lam, M.M. Savalani, S.-H. Teoh, D.W. Hutmacher, Dynamics ofin vitropolymer degradation of polycaprolactone-based scaffolds: accelerated versus simulated physiological conditions, Biomed. Mater. 3 (3) (2008) 034108.
[102] W.J. Cook, J.A. Cameron, J.P. Bell, S.J. Huang, Scanning electron microscopic visualization of biodegradation of polycaprolactones by fungi, Journal of Polymer Science: Polymer Letters Edition. 19 (4) (1981) 159–165.
[103] M. Mochizuki, M. Hirano, Y. Kanmuri, K. Kudo, Y. Tokiwa, Hydrolysis of polycaprolactone fibers by lipase: effects of draw ratio on enzymatic degradation, J. Appl. Polym. Sci. 55 (2) (1995) 289–296.
[104] A. Göpferich, Mechanisms of polymer degradation and erosion, Biomaterials. 17 (2) (1996) 103–114.
[105] M.-H. Huang, S. Li, M. Vert, Synthesis and degradation of PLA–PCL–PLA triblock copolymer prepared by successive polymerization of ε-caprolactone and dl-lactide, Polymer. 45 (26) (2004) 8675–8681.
[106] A. Yeo, B. Rai, E. Sju, J.J. Cheong, S.H. Teoh, The degradation profile of novel, bioresorbable PCL–TCP scaffolds: an in vitro and in vivo study, J. Biomed. Mater. Res. A 84A (1) (2008) 208–218.
[107] F. Karimi, A.J. O'Connor, G.G. Qiao, D.E. Heath, Integrin clustering matters: a review of biomaterials functionalized with multivalent integrin-binding ligands to improve cell adhesion, migration, differentiation, angiogenesis, and biomedical device integration, Advanced Healthcare Materials. 7 (12) (2018) 1701324.
[108] Y. Choi, S.Y. Cho, D.J. Park, H.H. Park, S. Heo, H.-J. Jin, Silk fibroin particles as templates for mineralization of calcium-deficient hydroxyapatite, J. Biomed. Mater. Res. B Appl. Biomater. 100B (8) (2012) 2029–2034.
[109] I. Deen, F. Rosei, Silk fibroin-derived polypeptides additives to promote hydroxyapatite nucleation in dense collagen hydrogels, PLoS One 14 (7) (2019) e0219429.
[110] R. Kino, T. Ikoma, S. Yunoki, N. Nagai, J. Tanaka, T. Asakura, et al., Preparation and characterization of multilayered hydroxyapatite/silk fibroin film, J. Biosci. Bioeng. 103 (6) (2007) 514–520.
[111] X.D. Kong, F.Z. Cui, X.M. Wang, M. Zhang, W. Zhang, Silk fibroin regulated mineralization of hydroxyapatite nanocrystals, J. Cryst. Growth 270 (1) (2004) 197–202.
[112] B. Marelli, C.E. Ghezzi, A. Alessandrino, J.E. Barralet, G. Freddi, S.N. Nazhat, Silk fibroin derived polypeptide-induced biomineralization of collagen, Biomaterials. 33 (1) (2012) 102–108.

[113] G.M. Nogueira, R.F. Weska, W.C. Vieira Jr., B. Polakiewicz, A.C.D. Rodas, O.Z. Higa, et al., A new method to prepare porous silk fibroin membranes suitable for tissue scaffolding applications, J. Appl. Polym. Sci. 114 (1) (2009) 617–623.
[114] Nogueira GM, Aimoli CG, Weska RF, Nascimento LS, Beppu MM. In Vitro Calcification of Silk Fibroin Hydrogel. Key Engineering Materials. 2008;361–363:503–6.
[115] P. Naserzadeh, S.A. Mortazavi, K. Ashtari, E. Seydi, J. Pourahmad, Evaluation of the toxicity effects of silk fibroin on isolated fibroblast and huvec cells, Iran J Pharm Res. 17 (Suppl2) (2018) 134–145.
[116] K. Numata, S. Yamazaki, N. Naga, Biocompatible and biodegradable dual-drug release system based on silk hydrogel containing silk nanoparticles, Biomacromolecules. 13 (5) (2012) 1383–1389.